Enhancing the electrocatalytic activity and stability of Prussian Blue Analogues through the introduction of Au nanoparticles in a core@shell heterostructure

Roger Sanchis-Gual, Toribio F. Otero, Marc Coronado-Puchau,* Eugenio Coronado*

R. Sanchis-Gual, Dr. M. Coronado-Puchau, Prof. E. Coronado
Instituto de Ciencia Molecular (ICMol)
Universidad de Valencia,
C/ Catedrático José Beltrán 2, Paterna, 46980, Spain
E-mail: marc.coronado@uv.es, eugenio.coronado@uv.es

Prof. T. F. Otero
Centre for Electrochemistry and Intelligent Materials (CEMI)
Universidad Politécnica de Cartagena
Aulario II, Paseo Alfonso XIII, E-30203 Cartagena, Murcia, Spain

Prussian blue analogues (PBAs) have shown to be useful as earth-abundant electrocatalysts for the Oxygen Evolution Reaction (OER) in acidic, neutral and alkaline media. Still, further improvements can be achieved by increasing their electrical conductivity. In this work, we have obtained and fully characterized a variety of monodisperse core@shell hybrid nanoparticles of Au@PBA (PBA of $Ni^{II}Fe^{II}$ and $Co^{II}Fe^{II}$) with different shell sizes. Their electrocatalytical activity is evaluated by studying the OER, which is compared to the pristine PBA and other Au-PBA heterostructures. It was observed that the introduction in a core@shell of 5-10 % of Au in weight leads to an increment in the electroactive mass able to be reduced or oxidized and thus, to a higher number of sites capable to take part in the OER. This larger amount of electroactive sites leads to a significant decrease in the onset potential (a reduction of the onset potential up to 100 mV and an increase up to 420 % of the current density recorded at an overpotential of 350 mV), while the Tafel slope remains unchanged, suggesting that Au reduces the limiting potential of the catalyst with no variation in the reaction kinetics. These effects are not experimented in the other Au-PBA nanostructures mainly due to the lower contact between both compounds and the oxidation of Au. Hence, an Au core activates the PBA shell and

increases the conductivity of the resulting hybrid while the PBA shell prevents Au oxidation. These improvements come from the strong synergistic effect existing in the core@shell structure and evidence the importance of the chemical design for preparing PBA-based nanostructures displaying better electrocatalytic performances and higher electrochemical stabilities.

1. Introduction

The electrolysis of water to produce hydrogen and oxygen offers the exciting possibility of storing energy whose importance is out of question today. However, this process requires high voltages mainly due to the slow kinetics of the oxygen evolution reaction (OER). This reaction represents a significant efficiency loss in water-splitting systems and often requires anode catalyst to reduce the energy barriers of the OER. In this context, earth-abundant electrocatalysts have been extensively studied in alkaline media.[1–3] First-row transition metal oxides of Co, Fe, or Ni show extremely high activities but only at very high pH (above 13), where the corresponding half-cell reduction reaction (for example, the hydrogen production) is more difficult. Nevertheless, at lower pH, most of the catalysts suffer corrosion. Thus, an efficient catalyst for OER at acidic or near-neutral solution based on earth-abundant metals remains an important challenge. In such conditions, benchmark materials are principally based on Ir or Ru oxides, affecting considerably the cost of this technology.[4,5]

Prussian blue analogues (PBA) are coordination polymers based on bimetallic cyanide complexes of general formula $A_aB_b[D(CN)_6]_d$ (A = alkali cation, B, and D = transition metal ions).[6] These materials are of interest in this context since they are robust, chemically tuneable, based on earth-abundant metals and they exhibit large specific surface areas. In fact, they have recently been investigated as an interesting implementation in multifunctional materials for many energy-related fields, such as supercapacitors, sodium-ion batteries and electrocatalysts.[7–10] Moreover, well-stabilized PBAs are robust and stable in a large pH range

2

exhibiting catalytic activities comparable to those of metal oxides for OER.[10] However, PBAs exhibit low electrical conductivities, which increase the required overpotentials in water splitting.[11] For this reason, the combination of PBA with other nanomaterials has attracted considerable attention in order to further improve their electrocatalytic activity.[10,12]

Recent studies have shown that electrocatalysts based on Co, Ni and Fe are oxidized before the onset of oxygen evolution, being the oxidized metals the active species in the pathway for O_2 evolution.[13–15] Thus, a possibility to enhance the electrocatalytic activity could be done by combining efficient electrocatalysts with highly electronegative metals. In this line, Au is the highest electronegative metal and thus it can drain electrons from the catalyst.[16,17] Besides, in combination with the electrocatalyst it may contribute to improve the electrocatalytic performance thanks to the increase in the conductivity of the resulting material.[18–20] To this aim, in this work we have explored the preparation of hybrid materials combining PBAs with Au. In particular, we have focused on nanoparticles (NPs) since they are usually the preferred form of catalysts due to the large number of electroactive sites provided by their high surface areas. Among them, the core@shell structure has been extensively used to obtain hybrid materials at the nanometer scale.[21,22] Still, Au@PBA heterostructure remains an unexplored hybrid material for electrocatalysis. Thus, Au@PBA heterostructures have been mostly focused on the pure Prussian blue compound $(A_aFe_x[Fe(CN)_6]_y)$.[23–27] Only recently, heterostructures with other metallic compositions such as NiFe and CoFe, which are interesting for OER, have been reported.[28,29]

The aim of this work is to study the influence of Au on the electrocatalytical activity of PBA. To do so, we have synthesized and fully characterized a variety of monodisperse core@shell NPs of Au@PBA (PBA of $Ni^{II}Fe^{II}$ and $Co^{II}Fe^{II}$) with an Au core diameter of *ca.* 15 nm and different shell sizes. The OER of these NPs has been systematically evaluated and compared to that of the pristine PBA and other Au-PBA heterostructures. By means of different techniques, we have analyzed the electroactive mass able to be oxidized or reduced, the active surface sites

and the resistances associated with the OER. We demonstrate that the existence of a strong synergistic effect between the core and the shell results in a large enhancement of the electrochemical performance and electrochemical stability of the hybrid Au@PBA heterostructures.

2. Preparation and characterization of the Au@PBA nanoparticles

2.1. Synthesis

The preparation of core@shell NPs of Au@PBA involves a two-step protocol in which $KAu(CN)_2$ reacts with KBH_4 in aqueous solution, reducing Au(I) to metallic Au, to afford Au NPs stabilized by cyanide groups (Au@CN NPs), followed in a second step by a dropwise addition of the PBA precursors to overgrow the PBA around the Au surface.[28,29] Still, this protocol needs further optimization to fulfill the requirements that are needed to make these hybrid Au@PBA NPs useful for electrocatalysis: (i) the amount of Au should be minimized with respect to that of the electroactive PBA shell since one needs to have the maximum number of electroactive sites while maintaining the beneficial properties of the Au core in terms of conductivity and activation of the shell (see below); (ii) a good coverage of the Au by the PBA shell to avoid its oxidation and dissolution during the electrochemical process; (iii) a good monodispersity in the size of the hybrid NPs to ensure the reproducibility in the electrochemical measurements.

With these considerations in mind, the first step in the preparation of Au@PBA NPs has been carried out at low temperature (around 10 °C). This temperature was set to induce the formation of smaller Au NPs and, consequently, to increase the surface area and the contact between Au and PBA. These NPs are in an equilibrium between borohydride (reducing agent) and cyanide (capping but also oxidizing agent). Furthermore, since KBH_4 leads to hydrogen bubbles that destabilize the Au NPs as a consequence of the water reduction,[30] in our protocol the $Au(CN)_2$:KBH_4 molar ratio was increased with respect to the original synthesis (from 0.08 to 0.25) to improve the Au monodispersity. This smaller NP size distribution was proved by the

width of the Au plasmon band (see below). On the other hand, in the specific case of Au@CoFe NPs, some additional changes need to be introduced to improve the CoFe coverage. Indeed, in this growth process, CoFe has a stronger tendency to self-nucleate than NiFe, as a consequence of the different kinetics.[31] For this reason, following the original protocol afforded an incomplete coverage of the Au NP by the overgrown shell (Figure S1A). To solve this problem, the precursors were added at lower rates in order to give enough time to the CoFe shell to grow better over Au (Figure S1B). Although a core@shell morphology is achieved at this point, a further improvement was still by varying the time delay (time between Au NPs formation and the beginning of the addition of the precursors). Thus, a higher time delay promotes the formation of single CoFe NPs (Figure S1C), while no time delay prevents the formation of well-stabilized Au@CN NPs (Figure S1D). A time delay of 10-20 min in combination with an addition rate of 0.5 mL·h^{-1} appears to be the most optimal conditions to get well stabilized Au NPs and thus, a well-defined shell growth around the metallic surface. Furthermore, PBA shell thickness can be controlled by varying the total PBA precursor volumes. Thus, after optimizing the protocol, we synthesized NPs perfectly covered by two limit shell sizes (*i.e.* a thin and a thick shell) to study their electrochemical performance (Figure 1).
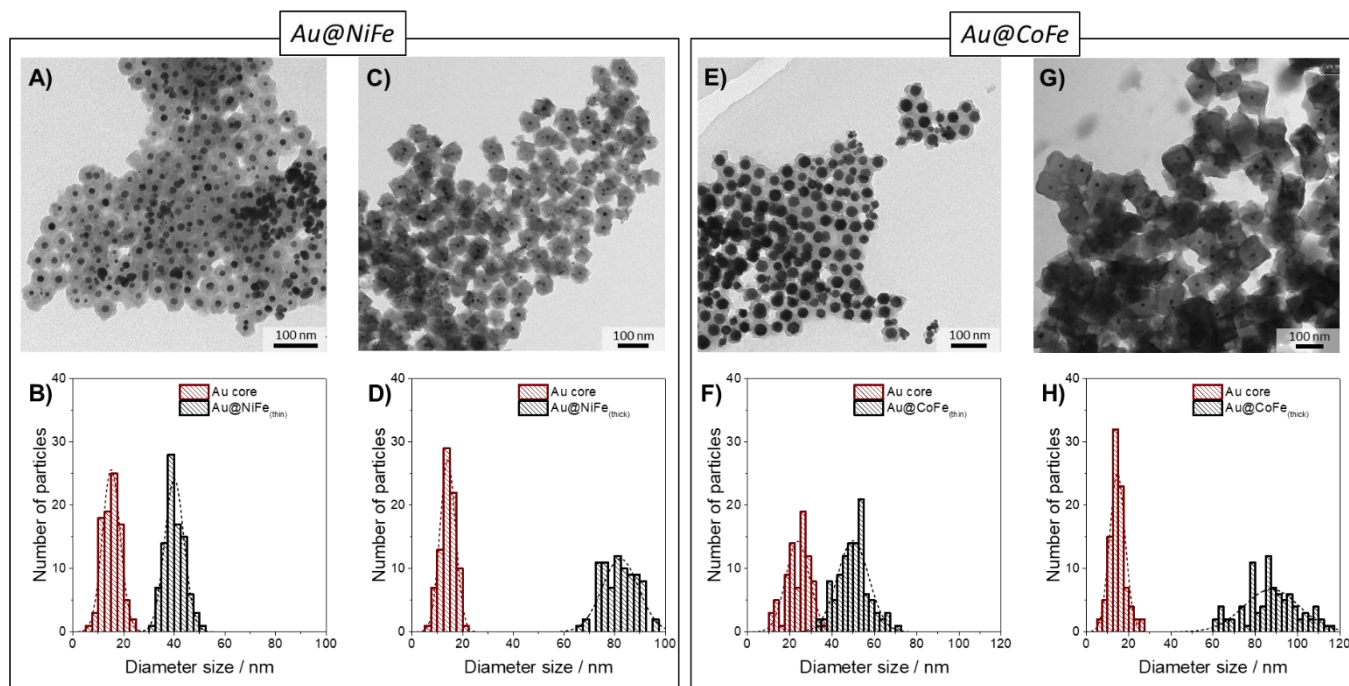
Figure 1. TEM images and histograms of the size distribution for Au@NiFe NPs with thinner (A, B) and thicker shells (C, D) and for Au@CoFe with thinner (E, F) and thicker shells (G, H).

2.2. Physical characterization

TEM images of the hybrid NPs show a core@shell morphology formed by an Au core and a well-defined PBA shell (Figure 1). For NiFe, hybrid NPs with shell thicknesses of 12 ± 2 and 30 ± 3 nm were prepared, while maintaining a constant size of about 15 nm for the Au core (Figure 1A to 1D). For CoFe, shell thicknesses of 13 ± 3 and 35 ± 6 nm have been obtained, but, in contrast to those of NiFe, the size of the Au core varies from 22 to 15 nm, respectively (Figure 1E to 1H). This core size difference could be a consequence of the major difficulties encountered in the CoFe system for growing the PBA layer around Au.

Interestingly, the Localized Surface Plasmon Resonance (LSPR) of the Au NPs is progressively red-shifted during shell formation (Figure S2). It can be attributed to the progressive change in the dielectric constant around the Au surface upon the continuous overgrowth of the shell.[32,33] It is expected that NiFe and CoFe exhibit quite similar values for the dielectric constant. Indeed, by comparing the red-shift shown by Au@PBA NPs with different shell thicknesses, one can

notice that for those having a 12-13 nm shell, a shift of *ca.* 21 nm is observed, while for those

having a 30-35 nm shell this shift turns out to be of *ca.* 28 nm. In addition, the full width at half

maximum (FWHM) of the plasmon band is slightly reduced after the PBA overgrowth. In point

of fact, the modification in the dielectric constant also leads to an increase in the plasmon band

intensity that decreases the FWHM (Figure S2). Moreover, the absence of other plasmon bands

together with the small width of these bands point toward a narrow size distribution for the Au

NPs. These plasmonic properties could be also beneficial for increasing the catalytic

performance by light irradiation since the increase in the local temperature could reduce even

more the onset potential and enhance the reaction rate.[34,35]

Energy-dispersive X-ray spectroscopy (EDX) demonstrates a homogeneous distribution of iron

and nickel, as well as iron and cobalt, over the Au NPs (see Figure S3). The estimated gold

content for the thinner and thicker shells is *ca.* 40 % and *ca.* 8%, respectively (see Table S1).

The molecular formulas estimated by Inductively Coupled-Plasma Optical Emission

Spectrometry (ICP-OES) can be found in the Supporting Information (Table S2). It is important

to note that these PBAs do not contain many vacancies (thus, few structural defects are

present[36]) since KBH_4 guarantees a high amount of potassium cations in the solution.

X-ray photoelectron spectroscopy (XPS) was performed on a powder of these NPs to get

information on the oxidation state of the metals contained in the PBA shells. For Au@NiFe,

nickel is present as Ni^{II}, while iron is reduced from Fe^{III} to Fe^{II} (Figure S4). This is in good

agreement with previous works reported in the literature[28] and with the magnetic

measurements. Indeed, while pristine $Ni^{II}Fe^{III}$ PBA behaves as a magnet below *ca.* 20 K,[37] the

Au@NiFe NPs stay paramagnetic down to 2 K (Figure S5) as a consequence of the reduction

of Fe^{III} (with S = 1/2) to Fe^{II} (with S = 0). Similarly, while pristine $Co^{II}Fe^{III}$ PBA exhibits

magnetic ordering below 14 K,[37] Au@CoFe remains paramagnetic at lower temperatures

(Figure S5). Such a reduction is promoted by KBH_4, which is still present in the solution. A

high concentration of this strong reductant is required to reach an equilibrium between the Au

7

reduction and the oxidation by cyanide. Lower amounts lead to non-stabilized Au NPs that can precipitate. Even though the presence of Fe^{II}, the Au@PBA heterostructures maintain the characteristic PB cubic structure in the XRDP data and the expected cyanide vibration in the Raman spectra, located at *ca.* 2150 cm^{-1} (see Figure 2).
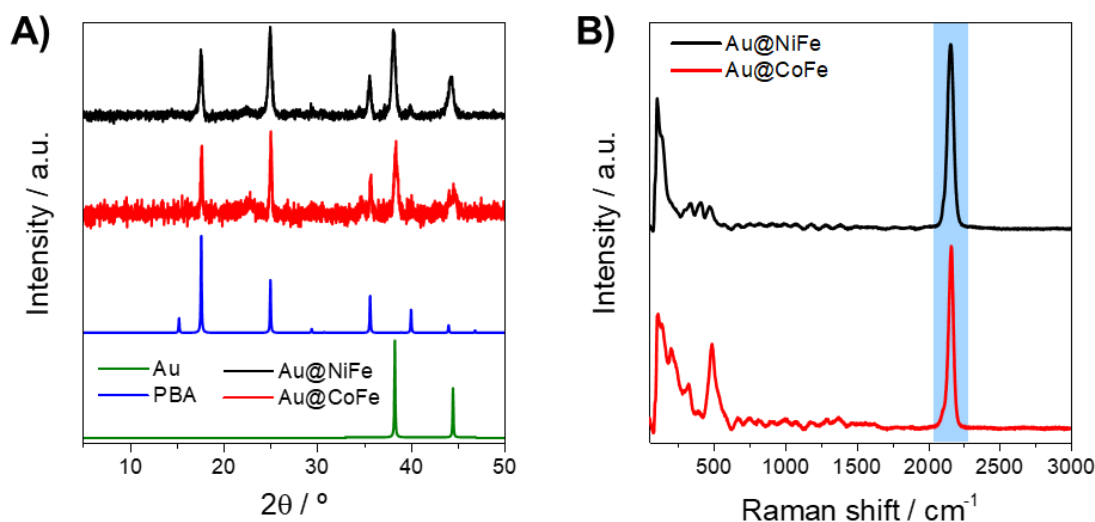

Figure 2. A) XRDP and B) Raman spectrum of the Au@PBA NPs. The cyanide vibration peak is highlighted in blue.

3. Electrochemical characterization

To verify the influence of Au on the electrochemical performance and the benefits of this sort of core@shell heterostructure, four kinds of NPs were also prepared: i) PBA NPs (NiFe^{III} and CoFe^{III}) containing many defects (*i.e.* many vacancies) since they give rise to higher electrocatalytic performance,[38] ii) PBA with reduced Fe^{II} (NiFe^{II} and CoFe^{II}) iii) PBA NPs decorated with Au NPs on its surface (Au-PBA)[39] and PBA NPs physically mixed with Au NPs (Au+PBA). TEM images of these systems and their respective histograms can be found in Figures S6-S9.

3.1. Evaluation of the Coulovoltammetric response

The different abovementioned nanostructures were tested as OER electrocatalysts. Prior to that, CV curves were examined to analyze the redox processes. The Au@NiFe NPs exhibit redox peaks in a similar position as those observed for PBA-NiFe NPs of similar size (around 1.2 – 1.5 V). These peaks are related to Ni processes (Figure S10).[40] In the CoFe case, all the studied NPs show a small redox couple between 1.2 and 1.4 V, which can be assigned to Co redox processes (Figure S11).[41] Observing the dependence of the charge on the applied potential, it can be noticed that NiFe compounds display almost reversible peaks (closed coulovoltammetric loops;[42,43] Figure S12), whereas, in CoFe compounds, an excess anodic charge was observed (open coulovoltammetric loops;[42,43] Figure S13). This irreversible charge comes from the lower onset potential of the OER; this leads to the irreversible formation of O_2 at the most anodic potential. As it is demonstrated here, this is a useful technique since it brings the possibility to separate charges consumed by electrodic redox processes from charges expended by irreversible electrocatalytic processes —as oxygen evolution here— when both processes overlap in the same potential range. Therefore, this technique can provide a deeper understanding of both the onset OER potential and the evolution of the oxygen production.[44] In this work, coulovoltammetry has been used to extract and analyze the reversible charges of the different compounds.

Remarkably, important differences in the current density and reversible charge are observed in the NPs, especially for the NiFe systems (Figures S10-S13). Thus, compared to the pristine NiFe^{III} and NiFe^{II}, the system Au@NiFe with a thin shell displays lower current density values, possibly due to the low content of electroactive NiFe material, which represents *ca.* 60% of the total mass. In fact, if one takes into account the electroactive mass for these three cases, the current density and the total charge coming from these redox processes are quite similar (see Figure S14), suggesting that the density values are controlled by the percentage of electroactive PBA. Interestingly, this rule is not followed for Au@NiFe NPs with a thick shell. Then, with around 90 % (in weight) of NiFe, the current densities are about 5 times greater for the

core@shell NPs as compared with those of the NiFe^{II} NPs and even with those of the pristine NiFe^{III} NPs. This strong and anomalous enhancement in the current density could be related to the increase in the conductivity of the hybrid material (compared with that of pristine PBA NPs), as well as with the number of electroactive sites. In this line, using Faraday's law of electrochemical reactions and the redox charges extracted from Figures S12 and S13, the total PBA mass involved in the redox processes was estimated. For pristine PBA, the PBA of Fe^{II} and Au@PBA(thin), it was found that the reduced or oxidized PBA mass is below 10 % of the total PBA electrodic mass (See Table S3), suggesting that only the surface of the PBA material is electrochemically active. Higher electroactive percentages of the PBA mass were estimated for the core@shell heterostructures with a thick shell. Indeed, compared to the PBA of Fe^{II}, in the case of Au@NiFe(thick), an increment in the mass of electroactive species of around 600 % was calculated, while for the Au@CoFe(thick) system, this increment was found to be around 300 %. These results are in good agreement with the increase of the electrochemical surface area (ECSA) for these compounds (Figure S15). Notice that the ECSA represents the number of electroactive sites in the catalyst.[45] Some studies have indicated that Au contributes remarkably to the enhancement of this parameter.[46] In our case and compared to the PBA of Fe^{II}, an increment in the number of electroactive species of around 350 % was calculated for Au@NiFe(thick), while this increment was found to be around 500 % for the Au@CoFe(thick) system. Here the role of Au is the activation of the PBA shell, facilitating the interaction between the oxidized/reduced species and the electrolyte thanks to the close contacts established in this kind of core@shell heterostructure between the Au core and the PBA shell. This fact is corroborated by comparing these results with the lower current densities obtained in systems where the contacts between the two components are much weaker (PBA NPs decorated with Au NPs, Au-PBA) or inexistent (physical mixture of both NPs, Au+PBA) (see Figures S10, S11 and S14). These compounds display ECSA values considerably higher than that of the PBA NPs because Au exhibits a huge ECSA by itself (value of 0.18 $\mu F \cdot cm^{-2}$) when

it is exposed to the electrolyte. Thus, the larger and activated PBA sites from core@shell heterostructure could be exploited in order to increase the number of sites contributing to electrocatalytic reactions such as the OER.

3.2. Electrocatalytical performance

Electrocatalytic activities of different NPs —with and without Au— were tested and compared by Linear Sweep Voltammetry (LSV) performed now at a slow scan rate in order to minimize capacitive currents (see Figures 3A and 4A). Figures 3B and 4B display a zoom of the starting catalytic region to evidence the electrocatalytic differences. It is important to remark that these curves were not corrected with the solution resistance (iR, with R = 3 ± 1 Ω) to make a fair comparison of the intrinsic electrocatalytic behavior of each sample. When we compare the polarization curves from the different PBA NPs of Fe^{II}, we observe that Au@PBA materials (both with thick and thin shells) display lower onset potentials, which are lower when the coating shell is thicker. The attained values are even better than those shown by the pristine PBA samples with many defects (NiFe and CoFe). On the other hand, both, Au-PBA and Au+PBA, do not result advantageous in terms of electrocatalysis. In these materials, Au is exposed to the electrolyte and their LSV resemble the one recorded for Au showing high oxidation overpotentials. In addition, it is important to remind at this point that in the Au-PBA case, a polymer is used to connect both systems. Then, the polymer matrix surrounding Au NPs decreases the conductivity of the heterostructure leading to a lower electrocatalytic performance compared to that shown by the physical mixture Au+PBA.

To analyze the electrocatalytic behavior, some key parameters were compared from the experimental voltammetric responses, namely: (1) overpotential required to get 10 mA·cm^{-2} (horizontal dotted lines, Figures 3A and 4A), (2) flowing current density at a constant overpotential of 350 mV (vertical dotted lines, Figures 3B and 4B) and (3) Tafel slopes. The overpotential required at 10 mA·cm^{-2} was chosen because it is the approximate current density

11

expected for a 10% efficient solar-to-fuels conversion device under 1 sun illumination.[47] Figures 3C and 4C evidence that a thin shell leads to lower overpotentials, with a further decrease when the shell thickness is increased. Indeed, this parameter is reduced from 465 mV to 426 and then to 375 mV for NiFe^{II}, Au@NiFe(thin) and Au@NiFe(thick), respectively. For CoFe^{II}, Au@CoFe(thin) and Au@CoFe(thick), the overpotential decreases from 405 mV to 380 and then to 357 mV, respectively. A similar trend was observed for the current densities flowing at a fixed overpotential of 350 mV (Figures 3D and 4D): for Au@NiFe(thick), the current density increases from 1.6 to 5.1 mA·cm^{-2} (*i.e.* an improvement of 320 %) and for Au@CoFe(thick), from 1.9 to 8.1 mA·cm^{-2} (*i.e.* an improvement of 420 %). Besides, the results obtained for Au@PBA with a thick shell exceed considerably the performance recorded for a highly defective pristine PBA (NiFe and CoFe). On the other hand, when Au is exposed to the electrolyte (Au-PBA and Au+PBA samples), the heterostructure does not seem to be electrocatalytic at these overpotentials (Figures 3A and 4A) even if they display superior ECSA (Figure S15). Therefore, the electrocatalytic enhancement is originated thanks to the presence of a larger number of activated PBA sites as it occurs in a thick PBA layer surrounding Au. Specifically, the introduction of Au in a core@shell structure yields to a reduction of the overpotential up to 100 mV and an increase up to 420 % of the current density recorded at an overpotential of 350 mV.
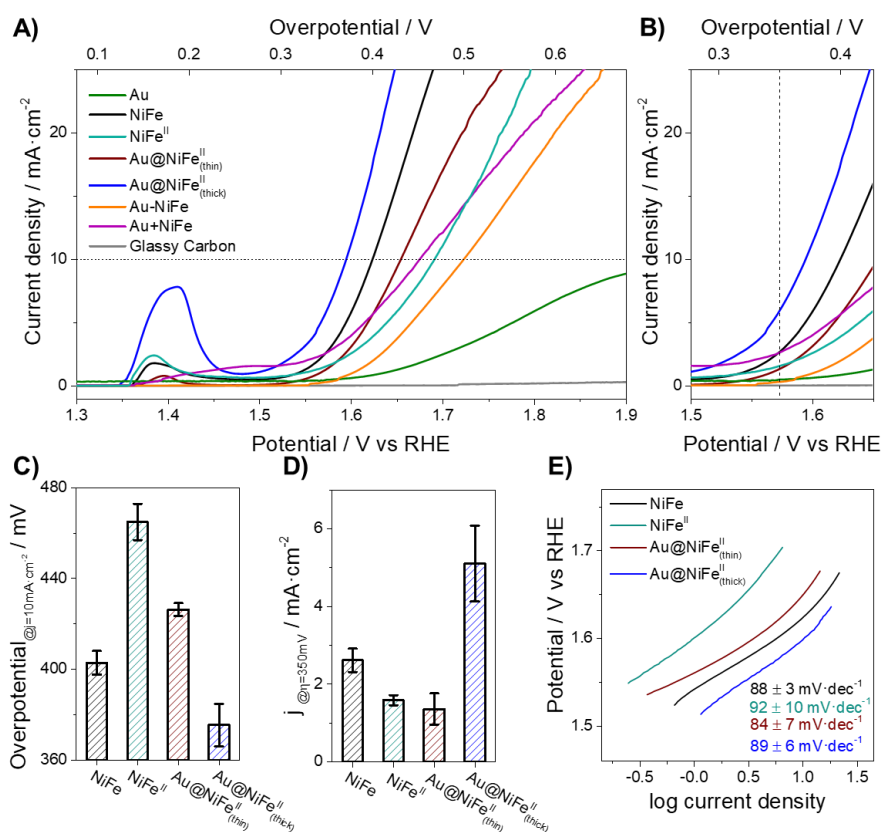
Figure 3. A) Linear Sweep Voltammetry of the different NiFe NPs measured at 5 mV·s⁻¹ in 1 M KOH aqueous solution. B) Zoom of Figure 4A exhibiting the beginning of the OER. C) Overpotential required for a current density of 10 mA·cm⁻² for NiFe NPs. D) Current density obtained at an overpotential of 350 mV for NiFe NPs. E) Tafel slopes calculated from LSV data for NiFe NPs.
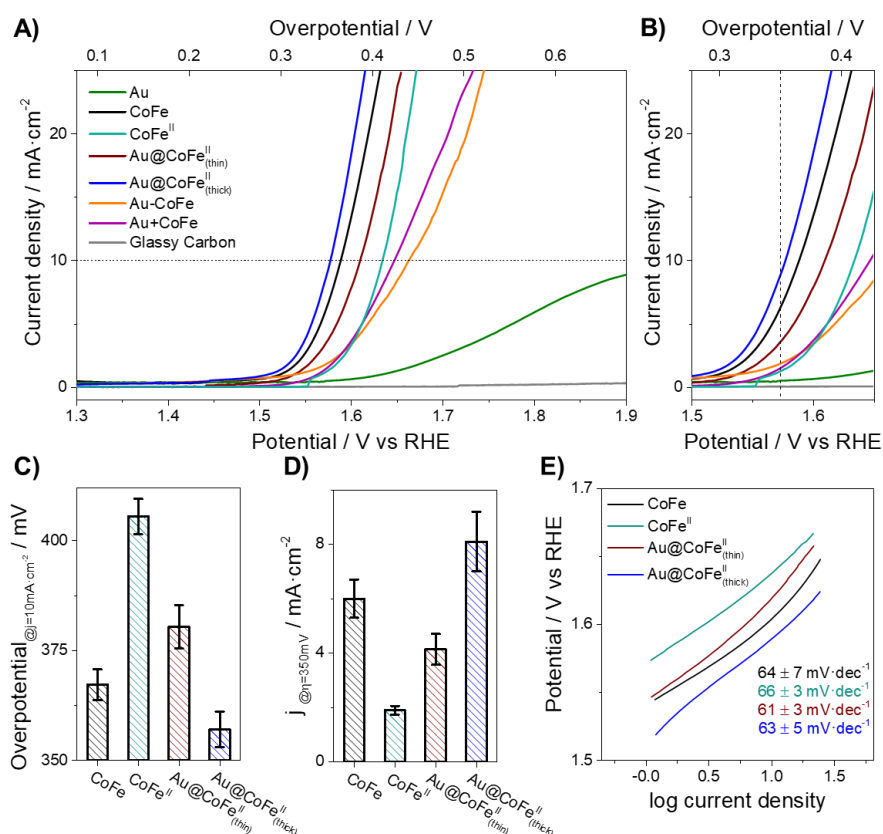
Figure 4. A) Linear Sweep Voltammetry of the different CoFe NPs measured at 5 mV·s^{-1} in 1 M KOH aqueous solution. B) Zoom of Figure 5A exhibiting the beginning of the OER. C) Overpotential required for a current density of 10 mA·cm^{-2} for CoFe NPs. D) Current density obtained at an overpotential of 350 mV for CoFe NPs. E) Tafel slopes calculated from LSV data for CoFe NPs.

Regarding the kinetics, Figures 3E and 4E show the Tafel slope values calculated from the LSV responses from NiFe and CoFe compounds, respectively. When Au oxidation is not taking place (either in the absence of Au or in the core@shell structure), similar Tafel slopes are observed, pointing to a small influence on both, the mechanism and kinetics of the oxygen release. Thus, the addition of Au decreases significantly the onset potential but it does not affect the Tafel slope, indicating that Au reduces the reaction overpotential without affecting the reaction kinetics. These results are in good agreement with those reported for other core@shell structures based on an Au core[16,48] supporting that this kind of nanostructure has a strong synergistic effect between the core and the shell. Trying to corroborate this point,

14

Electrochemical Impedance Spectroscopy (EIS) measurements were performed (Figures S16A and S16B).

The equivalent circuits used to fit the EIS data are shown in Figures S16C and S16D. Constant phase elements (CPEs), that are non-ideal capacitances, were introduced to provide a good match with the experimental data because of the possible surface roughness, physical non-uniformity and the non-uniform distribution of the electroactive sites. When PBA is the only species interacting with the electrolyte, the equivalent circuit is composed of a resistance coming from the ionic transport through the solution and the current collectors (R_s) connected in series with a first parallel branch (R_{int} and CPE_{int}) corresponding to the interfacial contact between the NPs and the Glassy Carbon. These three elements are observed in the high-frequency region. In the low-frequency region, OER processes occurring on the PBA surface are represented by a second parallel branch (R_{PBA} and CPE_{PBA}). As observed in Figure 5, R_{PBA} is significantly decreased due to the existence of defects in the PBA NPs, but an extraordinary drop is observed for the Au@NiFe heterostructures, leading to an enhancement of the electrocatalytic properties. As expected, a thinner PBA shell gives rise to lower resistance. Still, the incorporation of 5-10 % of Au is enough to reduce this resistance by 4 for NiFe and by 3 in CoFe.
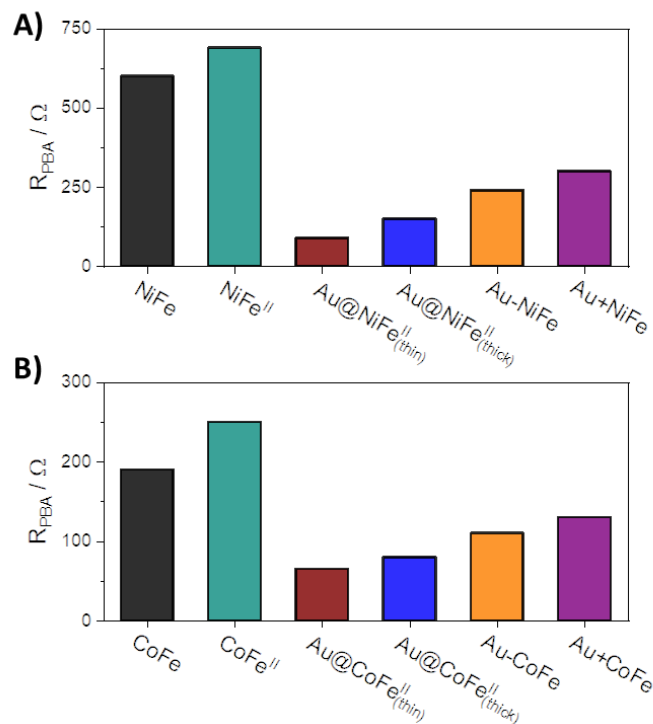
Figure 5. Resistance values of the PBA associated with the OER process for A) NiFe compounds and B) CoFe compounds. These resistance values were calculated from the equivalent circuit shown in Figure S16.

Summarizing, by comparing the different systems exhibiting the same Au loading (*i.e.* Au@PBA(thin), Au-PBA and Au+PBA), one can conclude that the appropriate design of the heterostructure is crucial in order to maximize the electrocatalytic activity. In fact, Au activates the PBA sites and increases the conductivity of the hybrid but must be protected to prevent its oxidation. In this case, the Au@PBA system turns out to be the most suitable nanoarchitecture. Here, a thick PBA layer further improves the catalytic performance thanks to the larger number of activated PBA sites acting on the OER and the still important increment in conductivity. Compared with previously reported OER electrocatalysts where their electrical conductivity was improved following different strategies to decrease the onset potential, our strategy turns out to be very effective (Table 1). Indeed, the introduction of small amounts of Au in a core@shell structure gives rise to a higher reduction of the voltage than using reduced graphene oxide (rGO). In addition to this, the overpotentials at 10 mA·cm^{-2} match the values obtained

16

for IrO_2 and are comparable to other reported electrocatalysts (Table S4). Furthermore, our electrocatalysts still display room for improvement since the electrochemical activity can be further improved by using other supporting electrodes (such as Ni foam) and by subjecting the heterostructures to different thermal and physical pretreatments (such as plasma activation).

Table 1. Comparison of overpotential improvement for the OER using previously reported strategies to increase the electrical conductivity of the electrocatalyst.

Sample comparison		Overpotential decrease at 10 mA·cm^{-2} (mV)	Reference
Au@NiFe	NiFe	92	This work
Au@CoFe	CoFe	51	This work
Au@CoO$_4$	CoO$_4$	50	[16]
ZnCo$_2$O$_4$/Au/CNTs	ZnCo$_2$O$_4$/CNTs	31	[46]
Au@NiO	NiO	90	[48]
Au@CoFeO$_x$	CoFeO$_x$	39	[48]
CNTs-Au@Co$_3$O$_4$	CNTs@Co$_3$O$_4$	50	[49]
Au/NiFe-LDH	NiFe-LDH	30	[50]
Ag+Co(OH)$_2$	Co(OH)$_2$	30	[51]
Ag@Co(OH)$_2$	Co(OH)$_2$	100	[51]
FeNi-rGO	FeNi	30	[52]
NiO-NiFe$_2$O$_4$/rGO	NiO-NiFe$_2$O$_4$	75	[53]
Co(OH)$_2$/SWNT	Co(OH)$_2$	40	[54]
Ni-Fe-Y-O$_x$ – Ni foam	Ni-Fe-Y-O$_x$ – GC	27	[55]

3.3. Electrochemical stability

Last but not least, the long-term stability of NiFe^{II} and CoFe^{II} with and without Au were compared for 24 hours under oxygen evolution at a constant current density of 20 mA·cm^{-2} (Figure 6). Note that Ni foam was used to avoid the detachment of the electrocatalyst from the electrode surface during the O_2 formation. The reaction overpotentials are lower than those expected from Figures 3 and 4 for the same current density, due to the porous structure of the substrate used to support the NPs in these measurements (Ni foam foil).[56] The best electrocatalytic stability was observed when introducing 5-10 % in weight of Au. Thus, after

24 hours of OER, the overpotential increment is 50 % lower in the core@shell NPs than when the Au is absent. It seems that Au gives rise to lower overpotentials which favors the long time stability of the PBA during the OER. It is worth noting that Au-PBA nanostructures exposing Au to the electrolyte exhibit a progressive voltage increase caused by Au oxidation and dissolution.
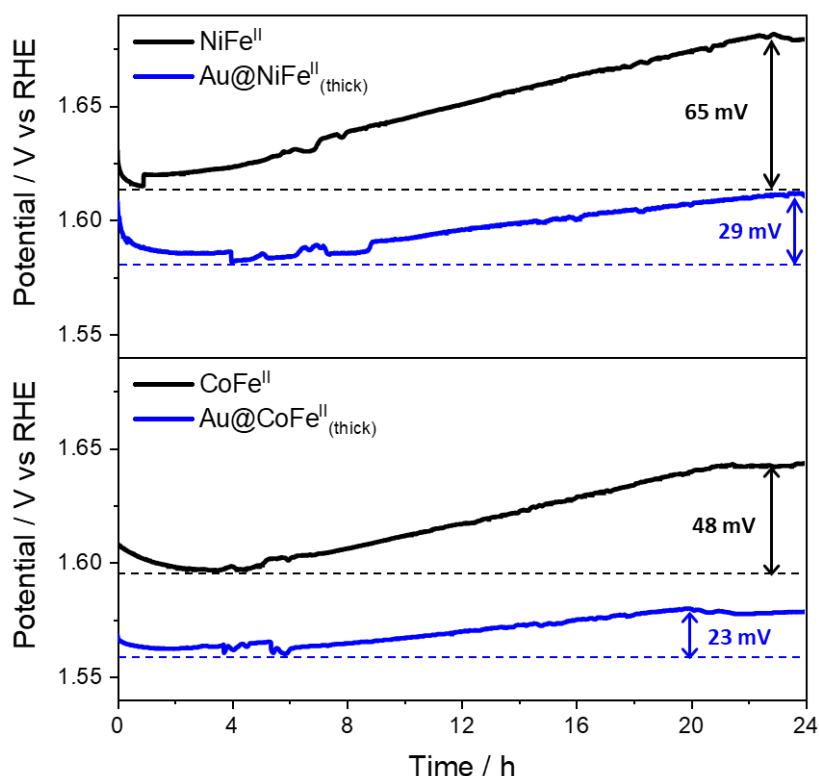

Figure 6. Stability of NiFe^{II} and CoFe^{II} with and without Au, under a constant current density of 20 mA·cm^{-2} for 24 h.

Coulovoltametric responses before and after the stability test can be analyzed to calculate the electroactive mass involved in the redox processes (including Ni foam). A reduction of the electroactive mass of around 32 % for NiFe^{II} but only 20 % for the Au@NiFe(thick) sample was found (Figure S17). For CoFe these values are 25 % and 15 %, respectively (Figure S18). The increment of the reaction overpotential is likely a consequence of the loss of electroactive mass caused by the physical detachment or the progressive inactivity of these electroactive centers. Accordingly, these results prove that a proper Au incorporation greatly enhances the

electrochemical activity of the electroactive PBA shell, improving at the same time its electrochemical stability. Along this front, a core@shell heterostructure with a good Au coverage is necessary to prevent its oxidation.

4. Conclusion

We have reported here a variety of narrow-size distributed core@shell NPs of Au@PBA (PBA = Prussian Blue Analogues of $Ni^{II}Fe^{II}$ and $Co^{II}Fe^{II}$) formed by an Au core and a PBA shell of different thicknesses. The electrocatalytical activity of such NPs has been evaluated and compared to some PBA and other Au-PBA nanostructures. Compared to the PBA without Au, it was found that the introduction of small amounts of Au (5-10 % in weight) in the core@shell structure gives rise to a reduction of the overpotentials at 10 mA·cm^{-2} up to 100 mV and an increase up to 420 % of the current density recorded at an overpotential of 350 mV compared to the PBA without Au. Moreover, these voltage decreases are higher than the ones using reduced graphene oxide. Additionally, the Tafel slope remains unaffected indicating that Au reduces the limiting potential of the catalyst with no variation in the kinetics of the reaction. It was detected for these heterostructures an important increment in the electroactive mass able to be reduced or oxidized and thus, being able to participate in the OER. This in combination with the higher conductivity of the hybrid leads to an enhancement of the electrocatalytic activity that improves at the same time its electrochemical stability. These effects are not observed in the other Au-PBA nanostructures mainly due to the lower contact between both compounds and the oxidation of Au. Therefore, a core@shell heterostructure with a good Au coverage is required in order to get a protective and electroactive layer of PBA. These improvements are a consequence of the strong synergistic effect between the core and the shell of the Au@PBA nanostructures, which is facilitated by the close contact between both components. This work illustrates the importance of the chemical design for preparing PBA-based nanostructures

exhibiting better electrocatalytic performances and higher electrochemical stabilities. In subsequent studies both, the electrochemical activity and stability of these materials will be further improved by different thermal and physical pretreatments. This will be facilitated, for example, by exploiting the plasmonic properties of Au, which will allow us to induce a photothermal effect in these nanostructures.

5. Experimental Section

Materials:

All chemical reagents were purchased and used without further purification. Potassium ferricyanide, gold (I) potassium cyanide, nickel (II) chloride hexahydrate, cobalt (II) chloride hexahydrate, potassium borohydride, Chloroauric acid, sodium citrate tribasic dehydrate, thiol polyethyleneglycole amine (HS-PEG$_{3.5K}$-NH$_2$), potassium hydroxide (99.99%) and Nafion (117 solution) were purchased from Sigma-Aldrich. Carbon black, acetylene 50% compressed, was obtained from Alfa Aesar (99.9%). Milli-Q water was obtained from a Millipore Milli-Q equipment.

Nanoparticles synthesis

To prepare Au@NiFe NPs, 0.20 mmol of potassium borohydride (KBH$_4$) was added to 100 mL of an aqueous 0.5 mM solution of K[Au(CN)$_2$] under vigorous stirring at around 10 ℃. After 20-30 min, aqueous solutions of K$_3$[Fe(CN)$_6$] (5.7 mM) and NiCl$_2$·6H$_2$O (5.0 mM) were added simultaneously at a rate of 2 mL·h^{-1} to the Au NPs solution under vigorous stirring. After completion of the addition, the solution was vigorously stirred for half an hour. In order to prepare Au@CoFe NPs, 0.20 mmol of KBH$_4$ was added to 100 mL of an aqueous 0.5 mM solution of K[Au(CN)$_2$] under vigorous stirring at around 10 ℃. 10-15 minutes after the solution turns red, aqueous solutions of K$_3$[Fe(CN)$_6$] (5.7 mM) and CoCl$_2$·6H$_2$O (5.0 mM) were

added simultaneously at an addition rate of 0.5 mL·h^{-1} to the Au NPs solution under vigorous stirring. After completion of the addition, the solution was vigorously stirred for half an hour. Core@shell NPs were washed with water (11000 rpm for 20 minutes) and finally were dried under vacuum. A thinner and a thicker shell were achieved by adding respectively 2 and 10 mL of each precursor solution. K[Au(CN)$_2$] reduction was carried out in an ice bath in order to produce smaller Au cores.

PBA-NiFe NPs of around 150 nm were synthesized at room temperature by adding, to 100 mL aqueous solution at 2 mL·h^{-1} rate, aqueous solutions of CoCl$_2$·6H$_2$O (5.0 mM, 7 mL) and K$_3$[Fe(CN)$_6$] (5.7 mM, 7 mL) were added simultaneously. PBA-CoFe NPs of around 180 nm were also synthesized at room temperature by adding, to 100 mL aqueous solution at 2 mL·h^{-1} rate, aqueous solutions of NiCl$_2$·6H$_2$O (5.0 mM, 8 mL) and K$_3$[Fe(CN)$_6$] (5.7 mM, 8 mL). After completion of the addition, the mixtures were stirred for half an hour before being centrifuged at 11000 rpm for 20 min. The supernatants were removed, and the powders were let dried under vacuum. PBA-NiFe^{II} and PBA-CoFe^{II} were prepared using the same synthetic procedure but adding 0.4 mmol of potassium borohydride (KBH$_4$) to promote the reduction of Fe^{III}.

Au NPs stabilized by citrate capping agent were synthesized following the well-known Turkevich method.[57] Physical mixture (Au+PBA) was prepared by joining in weight 30 % of Au NPs and 70 % of PBA NPs.

The decoration of Au on PBA NPs was carried out by connecting each NP by a polymer containing a thiol and an amine group(HS-PEG-NH$_2$) following a protocol developed in our group.[39]

Electrode preparation

For the electrode preparation, a dispersion composed of 1 mg of powder material, 0.5 mg of acetylene black, 200 µL of water and ethanol (1:1) and 8 µL of Nafion (10 %) was sonicated in order to obtain a well-dispersed suspension. Then, 3.6 µL was drop-casted in a previously

polished (sequentially with 1.0, 0.3 and 0.05 µm alumina powder) 3 mm Glassy Carbon electrode. Afterwards, the solvent was let evaporated at room temperature. The electrode mass loading achieved was around 0.25 mg·cm^{-2}.

Electrochemical measurements

Electrochemical tests were performed in a typical three-electrode cell equipped with Glassy Carbon acting as the working electrode and a platinum wire as the counter electrode. As the reference electrode, a silver-silver chloride (versus Ag/AgCl (3 M KCl)) was used. All potentials were converted referring to the oxygen evolution overpotential or the reversible hydrogen electrode (RHE). The measurements were performed at least three times for every sample using different electrodes on an Autolab PGSTAT 128N potentiostat/galvanostat. Linear sweep voltammetry (LSV) measurements were carried out at 5 mV·s^{-1} in a previously N$_2$ purged 1 M KOH aqueous solution. Prior to this, cyclic voltammetries (CVs) were performed at different scan rates (100, 50, 20 and 10 mV·s^{-1}).

Electrochemical surface area (ECSA) was acquired by measuring the current associated with double-layer capacitance from the scan rate dependence of CVs. The potential range used for the CVs was from -0.2 to 0.1 V versus Ag/AgCl (3 M KCl). The scan rates were 400, 300, 200, 100 and 50 mVs^{-1}. The double layer capacitance was estimated by plotting the (ja–jc) (anodic versus cathodic currents) at -0.05 V versus Ag/AgCl (3 M KCl) against the scan rate. The ECSA was measured on the working electrodes after performing an activation process consisting of 5 CVs at 50 mV·s^{-1} around their redox processes.

Electrochemical impedance spectroscopy (EIS) measurements were carried out using a Gamry 1000E potentiostat/galvanostat controlled by Gamry software by applying an AC amplitude of 10 mV in the frequency range of 10^{-1}–10^5 Hz at an overpotential of 0.4 V. EIS data were analyzed and fitted by means of Gamry Echem Analyst v. 7.07 software.

Stability tests were performed under a constant current density of 20 mA·cm^{-2} during 24 h using Ni foam foil (which area is 0.6 cm^2) as the working electrode containing 0.25 mg·cm^{-2} of electrocatalyst mass.

Physical characterization

UV/Vis Spectroscopy: UV-vis absorption spectra were recorded on a Jasco V-670 spectrophotometer in baseline mode from 300 to 900 nm range, using 1.000-cm-optical-path plastic cuvettes.

Inductively Coupled-Plasma Optical Emission Spectrometry (ICP-OES): The ICP-OES analysis were conducted at the Universidad de Valencia (Sección de Espectrometría Atómica y Molecular). Samples were digested in an acid medium at 220 ℃ using a microwave oven.

Transmission Electron Microscopy (TEM): TEM studies were carried out on a JEOL JEM 1010 microscope operating at 100 kV, and Technai G2 F20 microscope operating at 200 kV. Samples were prepared by dropping suspensions on lacey formvar/carbon copper grids (300 mesh).

Magnetic Measurements: Magnetic data were collected with a Quantum Design MPMS XL-5 susceptometer equipped with a SQUID sensor. Field Cooling magnetization measurements were performed under a magnetic field applied of 1000 Oe.

Raman Spectroscopy: Raman spectra were acquired with a Raman Emission Horiba-MTB Xplora Spectrometer in ambient conditions. NPs were measured with a laser wavelength of 532 nm by drop-casting the samples onto silicon substrates.

X-Ray Powder Diffraction (XRPD): X-ray powder diffraction (XRPD) patterns were obtained with a PANalytical X'Pert diffractometer using the copper radiation (Cu-Ka = 1.54178 Å) in the 5–50 region.

X-ray Photoelectron Spectroscopy (XPS): Samples were analyzed using a K-ALPHA Thermo Scientific spectrometer. All spectra were collected using Al Kα radiation (1486.6 eV), monochromatized by a twin crystal monochromator, yielding a focused X-ray spot (elliptical

in shape with a major axis length of 400 μm) at 30 mA and 2 kV. The alpha hemispherical analyzer was operated in the constant energy mode with survey scan pass energies of 200 eV to measure the whole energy band and 50 eV in a narrow scan to selectively measure the particular elements. XPS data were analyzed with Avantage software. A smart background function was used to approximate the experimental backgrounds. Charge compensation was achieved with the system flood gun that provides low energy electrons and low energy argon ions from a single source.

References

[1]   F. Song, L. Bai, A. Moysiadou, S. Lee, C. Hu, L. Liardet, X. Hu, *J. Am. Chem. Soc.* **2018**, *140*, 7748.

[2]   Z. P. Wu, X. F. Lu, S. Q. Zang, X. W. Lou, *Adv. Funct. Mater.* **2020**, *30*, 1.

[3]   G. Abellán, J. A. Carrasco, E. Coronado, J. Romero, M. Varela, *J. Mater. Chem. C* **2014**, *2*, 3723.

[4]   Z. Shi, X. Wang, J. Ge, C. Liu, W. Xing, *Nanoscale* **2020**, *12*, 13249.

[5]   F. Lyu, Q. Wang, S. M. Choi, Y. Yin, *Small* **2019**, *15*, 1.

[6]   M. Verdaguer, G. S. Girolami, *Magnetic Prussian Blue Analogues*, Vol. 36, **2005**.

[7]   M. Morant-Giner, R. Sanchis-Gual, J. Romero, A. Alberola, L. García-Cruz, S. Agouram, M. Galbiati, N. M. Padial, J. C. Waerenborgh, C. Martí-Gastaldo, S. Tatay, A. Forment-Aliaga, E. Coronado, *Adv. Funct. Mater.* **2017**, *1706125*, 1.

[8]   F. Zhao, Y. Wang, X. Xu, Y. Liu, R. Song, G. Lu, Y. Li, *ACS Appl. Mater. Interfaces*

2014, *6*, 11007.

[9]   L. Han, P. Tang, Á. Reyes-Carmona, B. Rodríguez-García, M. Torréns, J. R. Morante,

J. Arbiol, J. R. Galan-Mascaros, *J. Am. Chem. Soc.* **2016**, *138*, 16037.

[10]   L. M. Cao, D. Lu, D. C. Zhong, T. B. Lu, *Coord. Chem. Rev.* **2020**, *407*, 213156.

[11]   D. Y. Chung, S. Park, P. P. Lopes, V. R. Stamenkovic, Y.-E. Sung, N. M. Markovic, D.

Strmcnik, *ACS Catal.* **2020**, *10*, 4990.

[12]   D. Zhao, Y. Lu, D. Ma, *Molecules* **2020**, *25*, 2304.

[13]   F. Dionigi, P. Strasser, *Adv. Energy Mater.* **2016**, *6*, 1600621.

[14]   D. Friebel, M. W. Louie, M. Bajdich, K. E. Sanwald, Y. Cai, A. M. Wise, M. J. Cheng,

D. Sokaras, T. C. Weng, R. Alonso-Mori, R. C. Davis, J. R. Bargar, J. K. Nørskov, A.

Nilsson, A. T. Bell, *J. Am. Chem. Soc.* **2015**, *137*, 1305.

[15]   J. G. McAlpin, Y. Surendranath, M. Dincã, T. A. Stich, S. A. Stoian, W. H. Casey, D.

G. Nocera, R. D. Britt, *J. Am. Chem. Soc.* **2010**, *132*, 6882.

[16]   Z. Zhuang, W. Sheng, Y. Yan, *Adv. Mater.* **2014**, *26*, 3950.

[17]   B. S. Yeo, A. T. Bell, *J. Am. Chem. Soc.* **2011**, *133*, 5587.

[18]   S. Zou, M. S. Burke, M. G. Kast, J. Fan, N. Danilovic, S. W. Boettcher, *Chem. Mater.*

2015, *27*, 8011.

[19]   J. W. D. Ng, M. García-Melchor, M. Bajdich, P. Chakthranont, C. Kirk, A. Vojvodic,

T. F. Jaramillo, *Nat. Energy* **2016**, *1*, 1.

[20]   R. Torres-Cavanillas, R. Sanchis-Gual, J. Dugay, M. Coronado-Puchau, M. Giménez-

Marqués, E. Coronado, *Adv. Mater.* **2019**, *31*, 1900039.

[21]   M. B. Gawande, A. Goswami, T. Asefa, H. Guo, A. V. Biradar, D. L. Peng, R. Zboril,

R. S. Varma, *Chem. Soc. Rev.* **2015**, *44*, 7540.

[22]   S. Gong, Y. X. Zhang, Z. Niu, *ACS Catal.* **2020**, *10*, 10886.

[23]   L. Jing, X. Liang, Z. Deng, S. Feng, X. Li, M. Huang, *Biomaterials* **2014**, *35*, 5814.

[24]   Y. Yin, Q. Li, S. Ma, H. Liu, B. Dong, J. Yang, D. Liu, *Anal. Chem.* **2017**, *89*, 1551.

[25] J. D. Qiu, H. Z. Peng, R. P. Liang, J. Li, X. H. Xia, *Langmuir* **2007**, *23*, 2133.

[26] G. Fu, W. Liu, S. Feng, X. Yue, *Chem. Commun.* **2012**, *48*, 11567.

[27] X. Lu, Y. Li, X. Zhang, J. Du, X. Zhou, Z. Xue, X. Liu, *Anal. Chim. Acta* **2012**, *711*, 40.

[28] G. Maurin-Pasturel, J. Long, Y. Guari, F. Godiard, M. G. Willinger, C. Guerin, J. Larionova, *Angew. Chemie - Int. Ed.* **2014**, *53*, 3872.

[29] G. Maurin-Pasturel, E. Mamontova, M. A. Palacios, J. Long, J. Allouche, J. C. Dupin, Y. Guari, J. Larionova, *Dalt. Trans.* **2019**, *48*, 6205.

[30] B. H. Liu, Z. P. Li, *J. Power Sources* **2009**, *187*, 527.

[31] J. Liang, C. H. Li, D. R. Talham, *Cryst. Growth Des.* **2020**, *20*, 2713.

[32] M. M. Miller, A. A. Lazarides, *J. Phys. Chem. B* **2005**, *109*, 21556.

[33] K. M. Mayer, J. H. Hafner, *Chem. Rev.* **2011**, *111*, 3828.

[34] C. Wang, O. Ranasingha, S. Natesakhawat, P. R. Ohodnicki, M. Andio, J. P. Lewis, C. Matranga, *Nanoscale* **2013**, *5*, 6968.

[35] X. Zhang, Y. L. Chen, R. S. Liu, D. P. Tsai, *Reports Prog. Phys.* **2013**, *76*, 046401.

[36] H. J. Buser, A. Ludi, D. Schwarzenbach, W. Petter, *Inorg. Chem.* **1977**, *16*, 2704.

[37] S. Juszczyk, C. Johansson, M. Hanson, A. Ratuszna, G. Malecki, *J. Phys. Condens. Matter* **1994**, *6*, 5697.

[38] Z. Y. Yu, Y. Duan, J. D. Liu, Y. Chen, X. K. Liu, W. Liu, T. Ma, Y. Li, X. S. Zheng, T. Yao, M. R. Gao, J. F. Zhu, B. J. Ye, S. H. Yu, *Nat. Commun.* **2019**, *10*, 1.

[39] R. Sanchis-Gual, I. Susic,a R. Torres-Cavanillas, D. Arenas-Esteban, Sara Bals, T. Mallah, M. Coronado-Puchau, E. Coronado. *Submitted.*

[40] X. Su, Y. Wang, J. Zhou, S. Gu, J. Li, S. Zhang, *J. Am. Chem. Soc.* **2018**, *140*, 11286.

[41] S. Pintado, S. Goberna-Ferrón, E. C. Escudero-Adán, J. R. Galán-Mascarós, *J. Am. Chem. Soc.* **2013**, *135*, 13270.

[42] T. F. Otero, M. Alfaro, V. Martinez, M. A. Perez, J. G. Martinez, *Adv. Funct. Mater.*

2013, *23*, 3929.

[43]   T. F. Otero, *Electrochim. Acta* **2016**, *212*, 440.

[44]   R. Sanchis-Gual, A. Seijas-Da Silva, T. F. Otero, E. Coronado, G. Abellán. *Manuscript in Preparation*.

[45]   J. A. Carrasco, A. Harvey, D. Hanlon, V. Lloret, D. McAteer, R. Sanchis-Gual, A. Hirsch, F. Hauke, G. Abellán, J. N. Coleman, E. Coronado, *Chem. Commun.* **2019**, *55*, 3315.

[46]   H. Cheng, C. Y. Su, Z. Y. Tan, S. Z. Tai, Z. Q. Liu, *J. Power Sources* **2017**, *357*, 1.

[47]   C. C. L. Mccrory, S. Jung, I. M. Ferrer, S. M. Chatman, J. C. Peters, T. F. Jaramillo, *J. Am. Chem. Soc.* **2015**, *137*, 4347.

[48]   A. L. Strickler, M. Escudero-Escribano, T. F. Jaramillo, *Nano Lett.* **2017**, *17*, 6040.

[49]   Y. Fang, X. Li, Y. Hu, F. Li, X. Lin, M. Tian, X. An, Y. Fu, J. Jin, J. Ma, *J. Power Sources* **2015**, *300*, 285.

[50]   J. Zhang, J. Liu, L. Xi, Y. Yu, N. Chen, S. Sun, W. Wang, K. M. Lange, B. Zhang, *J. Am. Chem. Soc.* **2018**, *140*, 3876.

[51]   Z. Zhang, X. Li, C. Zhong, N. Zhao, Y. Deng, X. Han, W. Hu, *Angew. Chemie Int. Ed.* **2020**, *59*, 7245.

[52]   X. Long, J. Li, S. Xiao, K. Yan, Z. Wang, H. Chen, S. Yang, *Angew. Chemie* **2014**, *126*, 7714.

[53]   G. Zhang, Y. Li, Y. Zhou, F. Yang, *ChemElectroChem* **2016**, *3*, 1927.

[54]   D. McAteer, I. J. Godwin, Z. Ling, A. Harvey, L. He, C. S. Boland, V. Vega-Mayoral, B. Szydłowska, A. A. Rovetta, C. Backes, J. B. Boland, X. Chen, M. E. G. Lyons, J. N. Coleman, *Adv. Energy Mater.* **2018**, *8*, 1.

[55]   Q. Zhang, N. Liu, J. Guan, *ACS Appl. Energy Mater.* **2019**, *2*, 8903.

[56]   W. Zheng, M. Liu, L. Y. S. Lee, *ACS Energy Lett.* **2020**, *5*, 3260.

[57]   J. Turkevich, *Gold Bull.* **1985**, *18*, 125.

[58]   F. Song, X. Hu, *Nat. Commun.* **2014**, *5*, 1.

[59]   C.-H. Chuang, L.-Y. Hsiao, M.-H. Yeh, Y.-C. Wang, S.-C. Chang, L.-D. Tsai, K.-C. Ho, *ACS Appl. Energy Mater.* **2020**.

Supporting Information

Enhancing the electrocatalytic activity and stability of Prussian Blue Analogues through the introduction of Au nanoparticles in a core@shell heterostructure

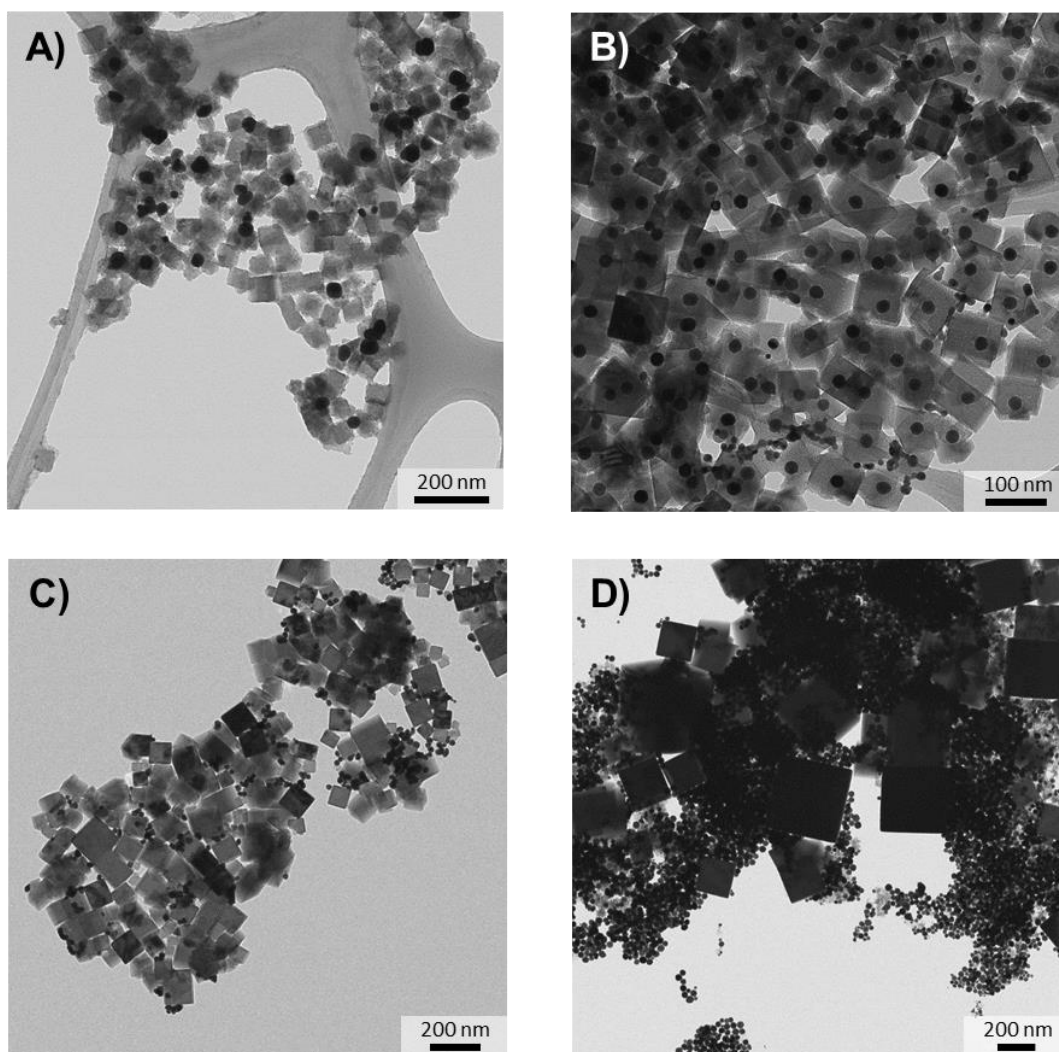*Roger Sanchis-Gual, Toribio F. Otero, Marc Coronado-Puchau,* Eugenio Coronado**

Figure S1. TEM images of the NPs obtained through the Au@CoFe protocol and applying the following parameters: A) addition rate of 2 mL·h⁻¹ and time delay of 20-30 min. B) addition rate of 0.5 mL·h⁻¹ and time delay of 20-30 min. C) addition rate of 0.5 mL·h⁻¹ and time delay of 45 min. D) addition rate of 0.5 mL·h⁻¹ and time delay of 0 min.
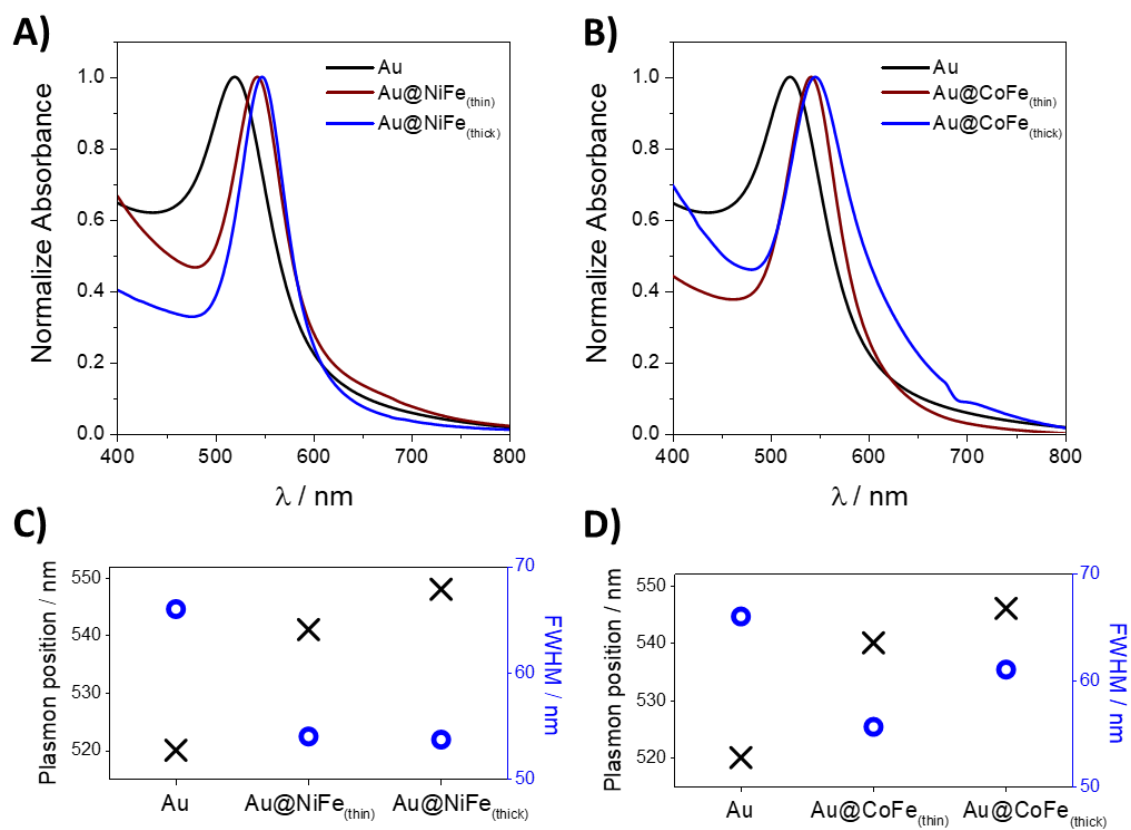
Figure S2. A) B) UV-Vis spectra of Au and the different Au@PBA NPs. C) D) Plasmon position and plasmon FWHM calculated for the different NPs.
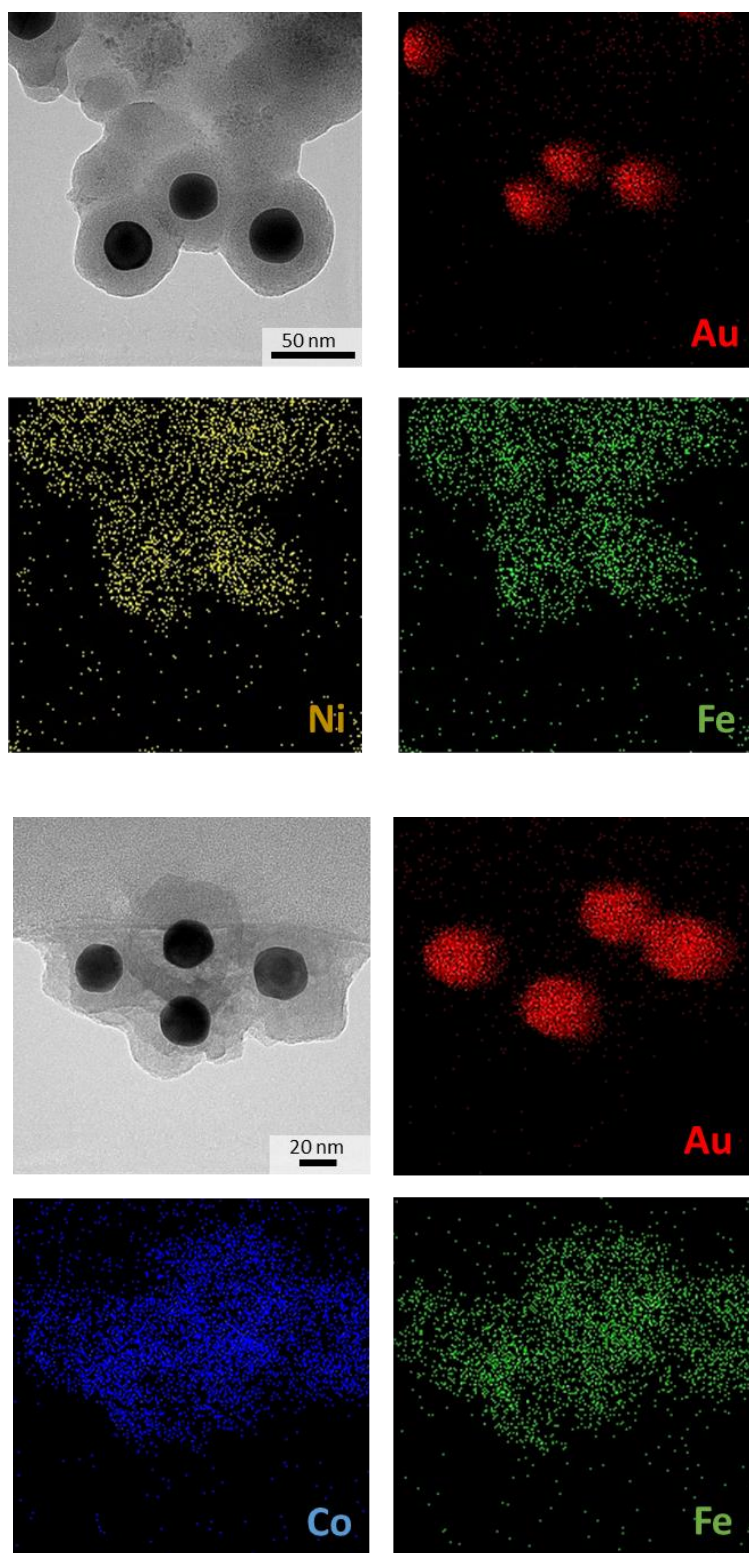
Figure S3. EDX mapping of the metals present in the Au@PBA(thin) heterostructures.

Table S1. Percentage of gold (in weight) estimated for the different nanoparticles.

Sample	% Au (w/w)
Au@NiFe^{II}(thin)	39
Au@NiFe^{II}(thick)	9
Au-NiFe	29
Au+NiFe	30
Au@CoFe^{II}(thin)	46
Au@CoFe^{II}(thick)	6
Au-CoFe	31
Au+CoFe	30

Table S2. Molecular formula estimated for the different nanoparticles.

Sample	Molecular formula
Au@NiFe^{II}(thin)	Au$_{0.88}$@K$_{1.60}$Ni[Fe(CN)$_6$]$_{0.90}$
Au@NiFe^{II}(thick)	Au$_{0.13}$@K$_{1.44}$Ni[Fe(CN)$_6$]$_{0.86}$
NiFe	K$_{0.20}$Ni[Fe(CN)$_6$]$_{0.72}$
NiFe^{II}	K$_{1.04}$Ni[Fe(CN)$_6$]$_{0.76}$
Au@CoFe^{II}(thin)	Au$_{1.10}$@K$_{1.52}$Co[Fe(CN)$_6$]$_{0.88}$
Au@CoFe^{II}(thick)	Au$_{0.05}$@K$_{1.56}$Co[Fe(CN)$_6$]$_{0.89}$
CoFe	K$_{0.19}$Co[Fe(CN)$_6$]$_{0.73}$
CoFe^{II}	K$_{1.12}$Co[Fe(CN)$_6$]$_{0.78}$
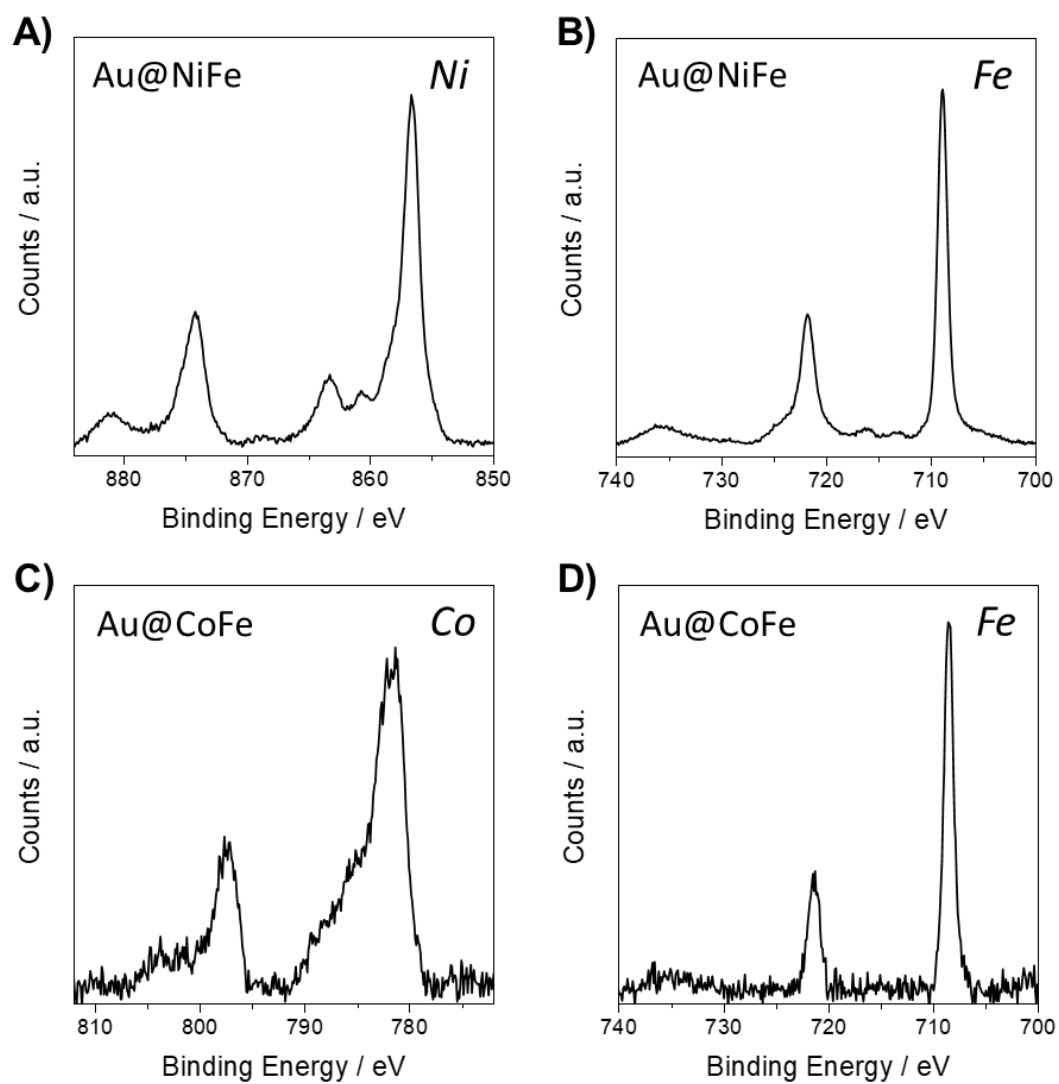
Figure S4. XPS spectra of Au@NiFe (up) and Au@CoFe (down).
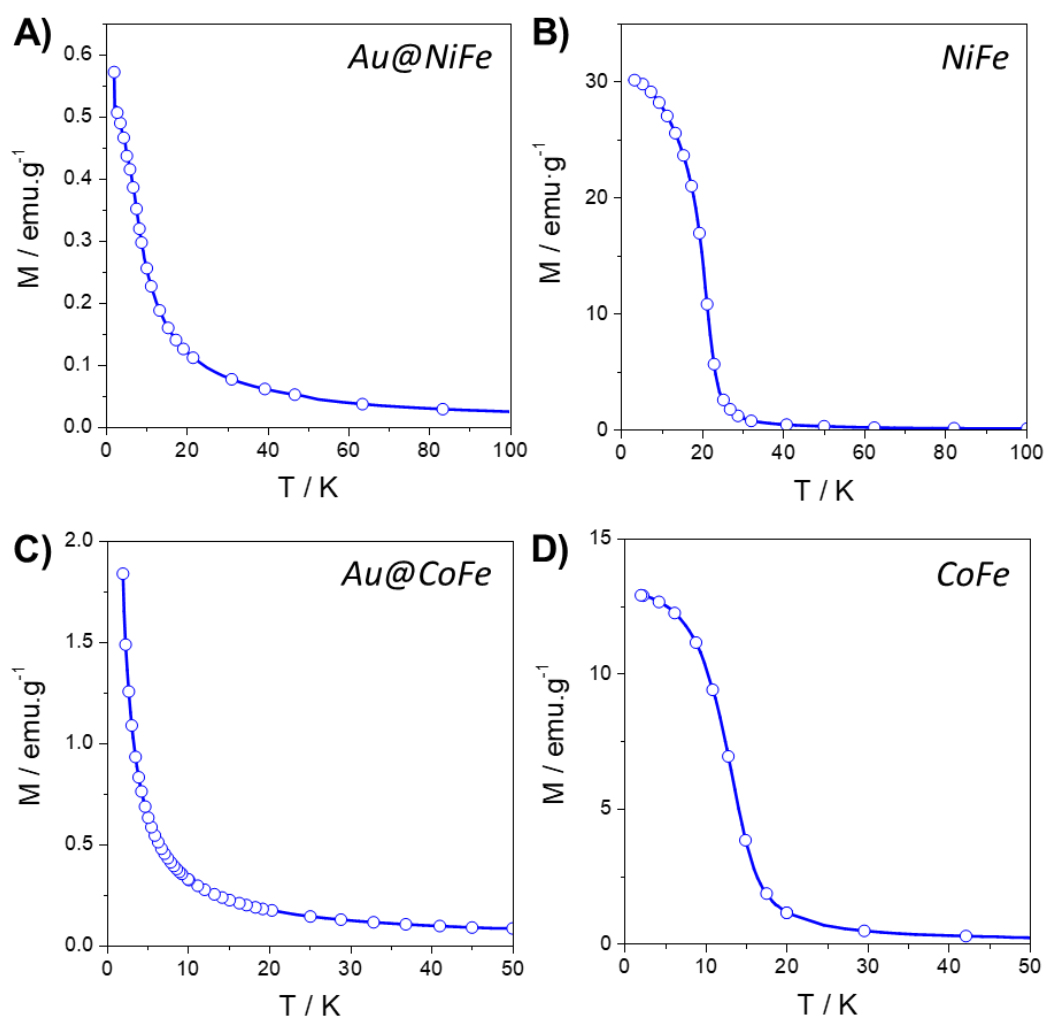
Figure S5. Magnetization vs. temperature curve performed for Au@NiFe and NIFe-PBA (up) and Au@CoFe and CoFe-PBA (down) nanoparticles with an applied field of 1000 Oe.
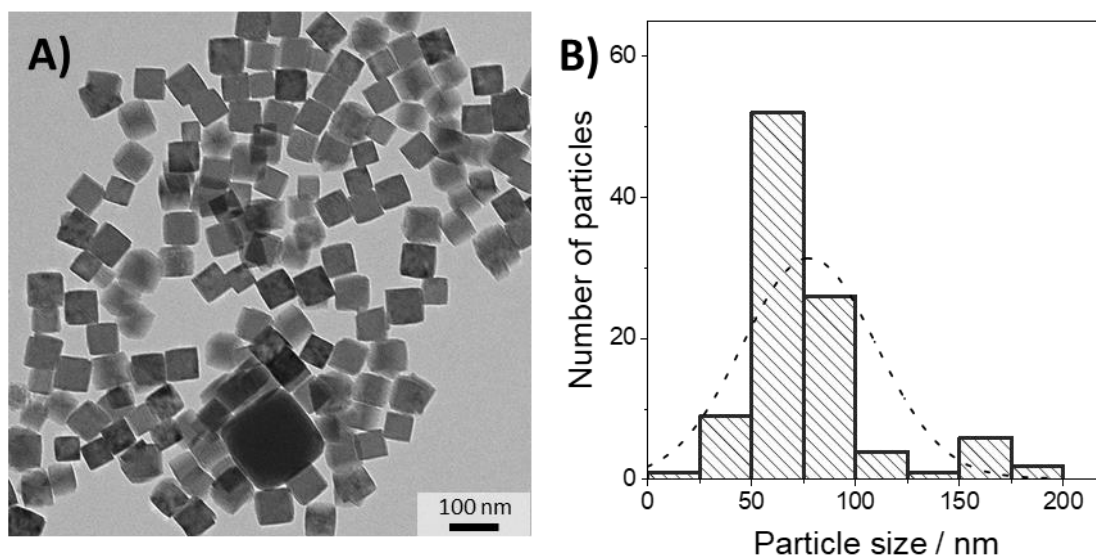
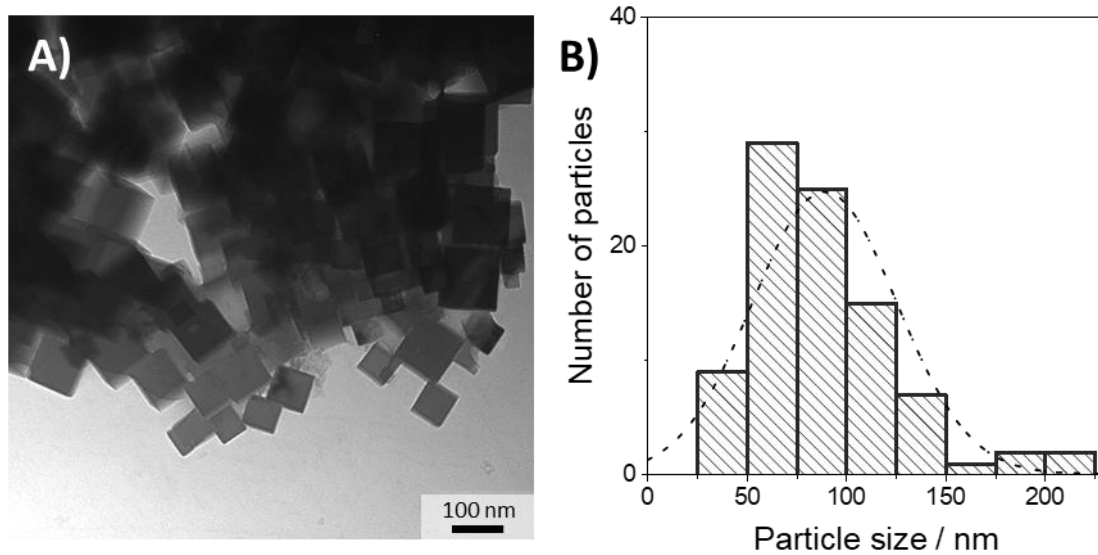**Figure S6.** PBA-NiFe^{II} NPs and its corresponding histogram.
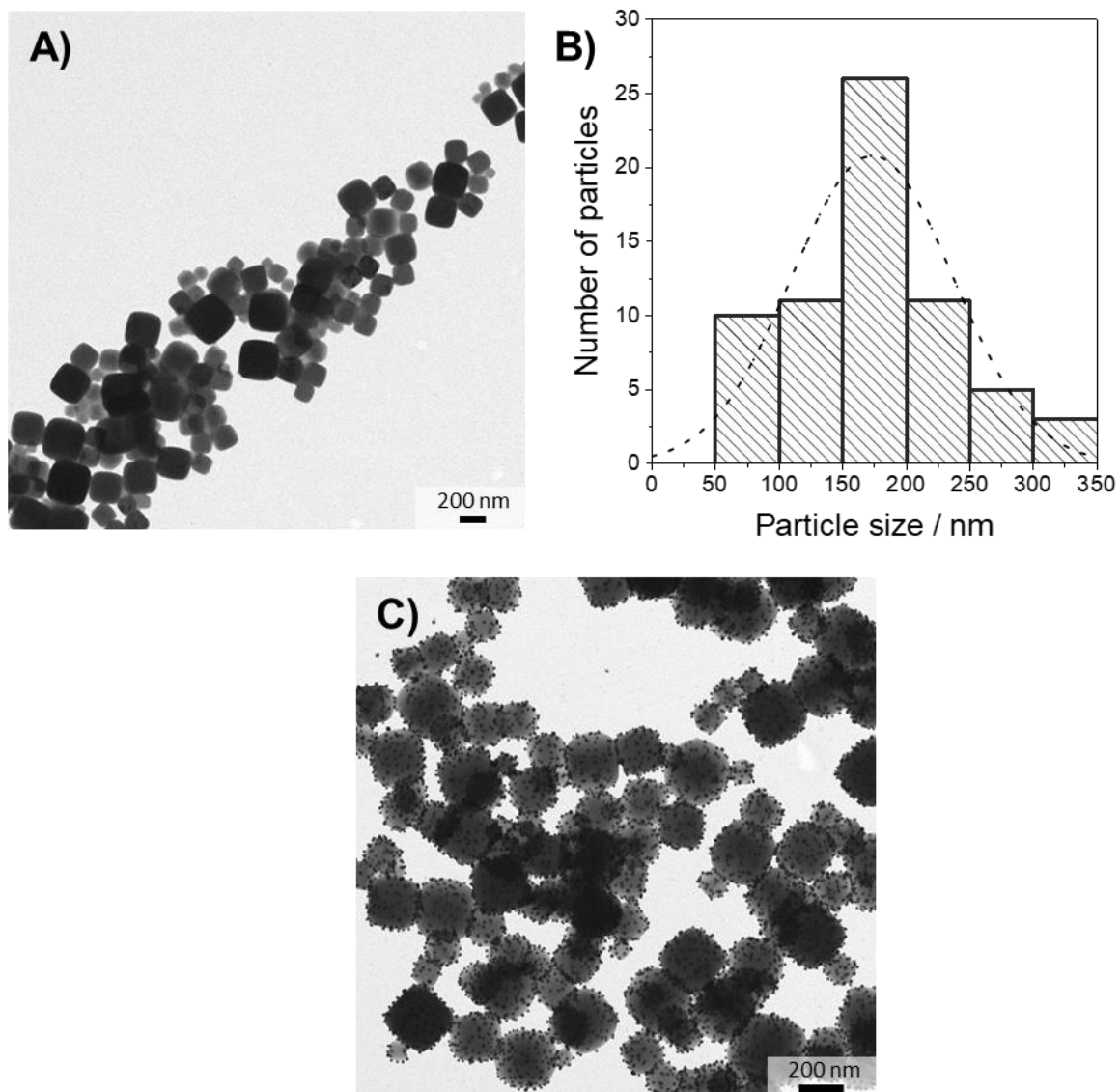
Figure S7. PBA-CoFe^{II} NPs and its corresponding histogram.

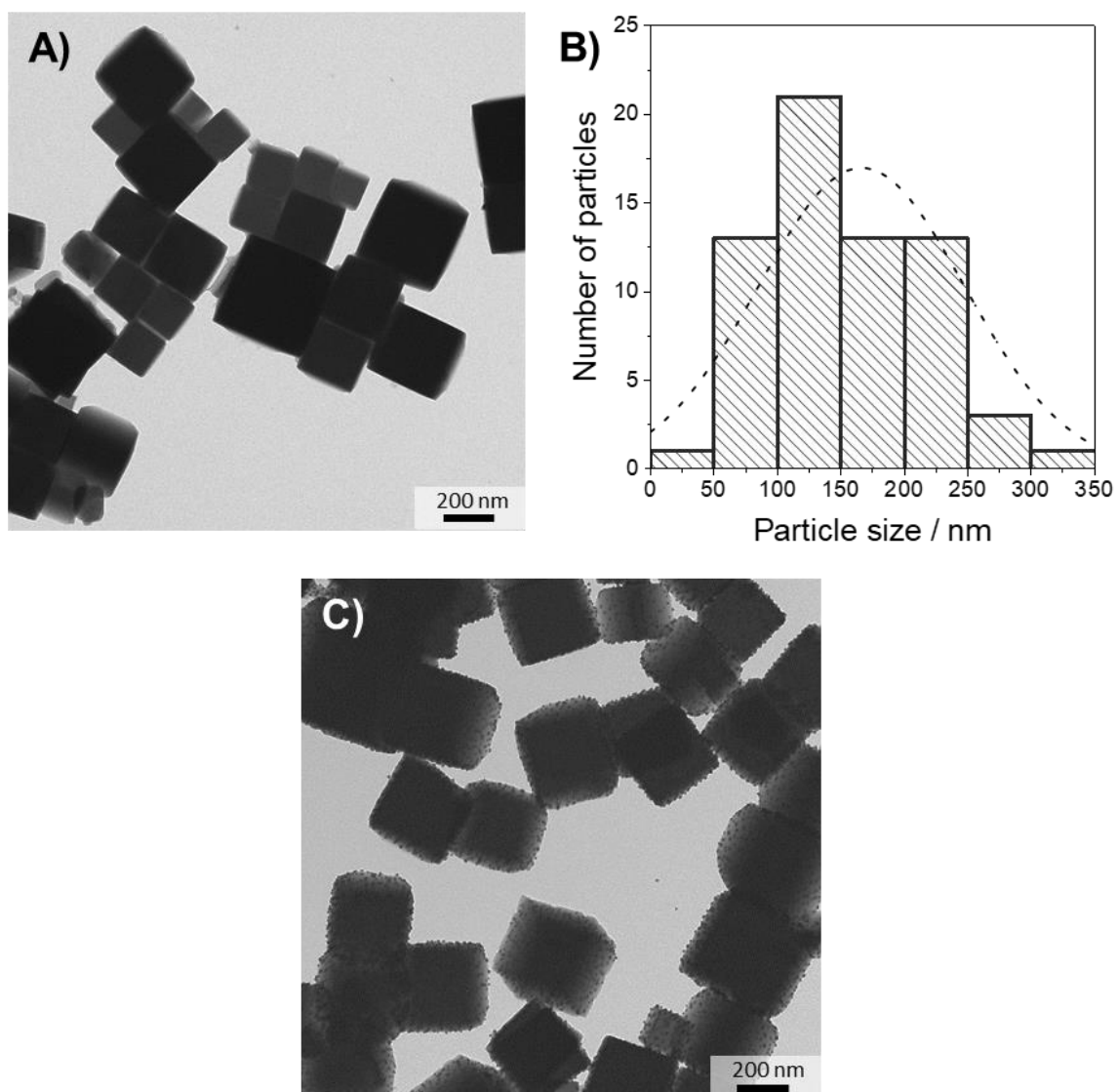**Figure S8.** A) B) PBA-NiFe NPs and its corresponding histogram. C) Au-decorated PBA-NiFe NPs.

Figure S9. A) B) PBA-CoFe NPs and its corresponding histogram. C) Au-decorated PBA-CoFe NPs.
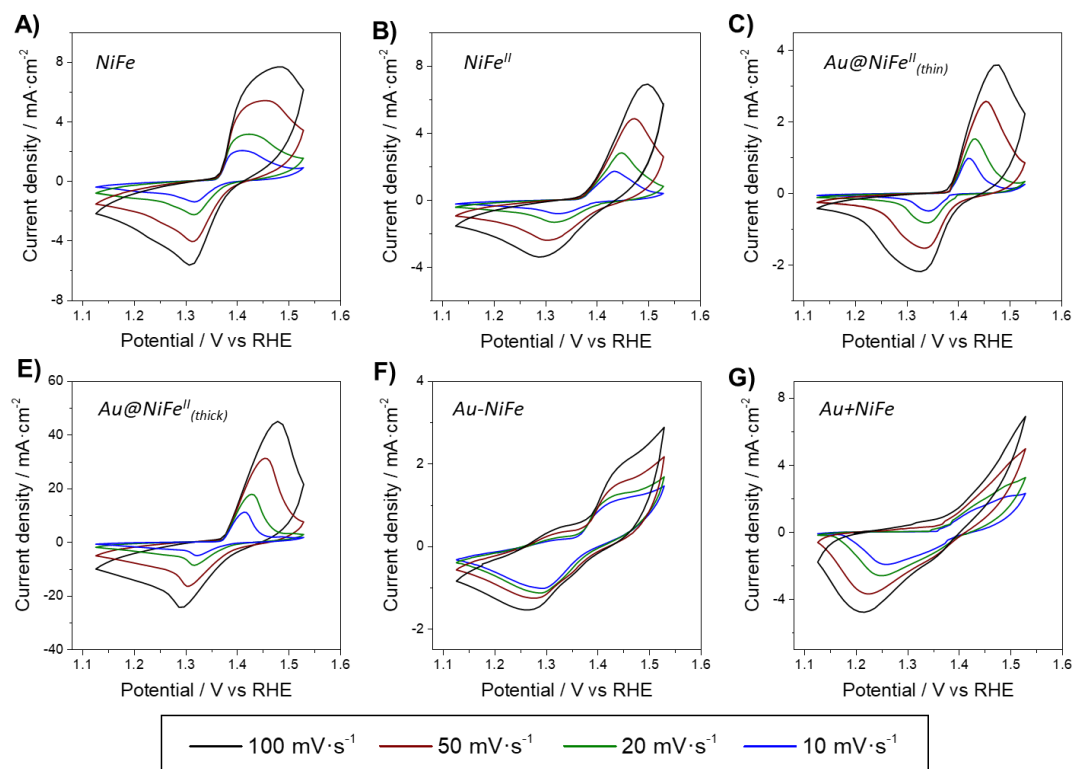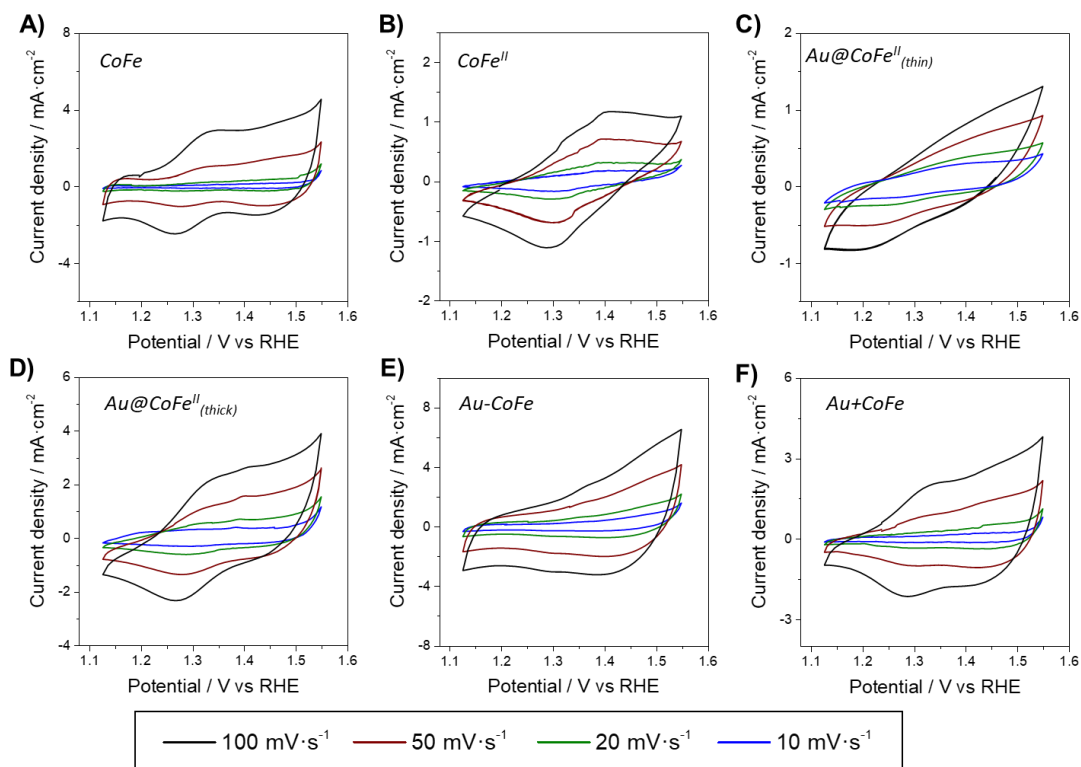
Figure S10. Voltammetric responses to potential cycles performed at different scan rates in 1 M KOH aqueous solution for different NiFe nanoparticles: A) PBA, B) PBA with Fe^{II}, C) Au@PBA (thin shell), D) Au@PBA (thick shell), E) Au decorated PBA NPs and F) physical mixture of Au and PBA NPs.

Figure S11. Voltammetric responses to potential cycles performed at different scan rates in 1 M KOH aqueous solution for different CoFe nanoparticles: A) PBA, B) PBA with Fe^{II}, C) Au@PBA (thin shell), D) Au@PBA (thick shell), E) Au decorated PBA NPs and F) physical mixture of Au and PBA NPs.
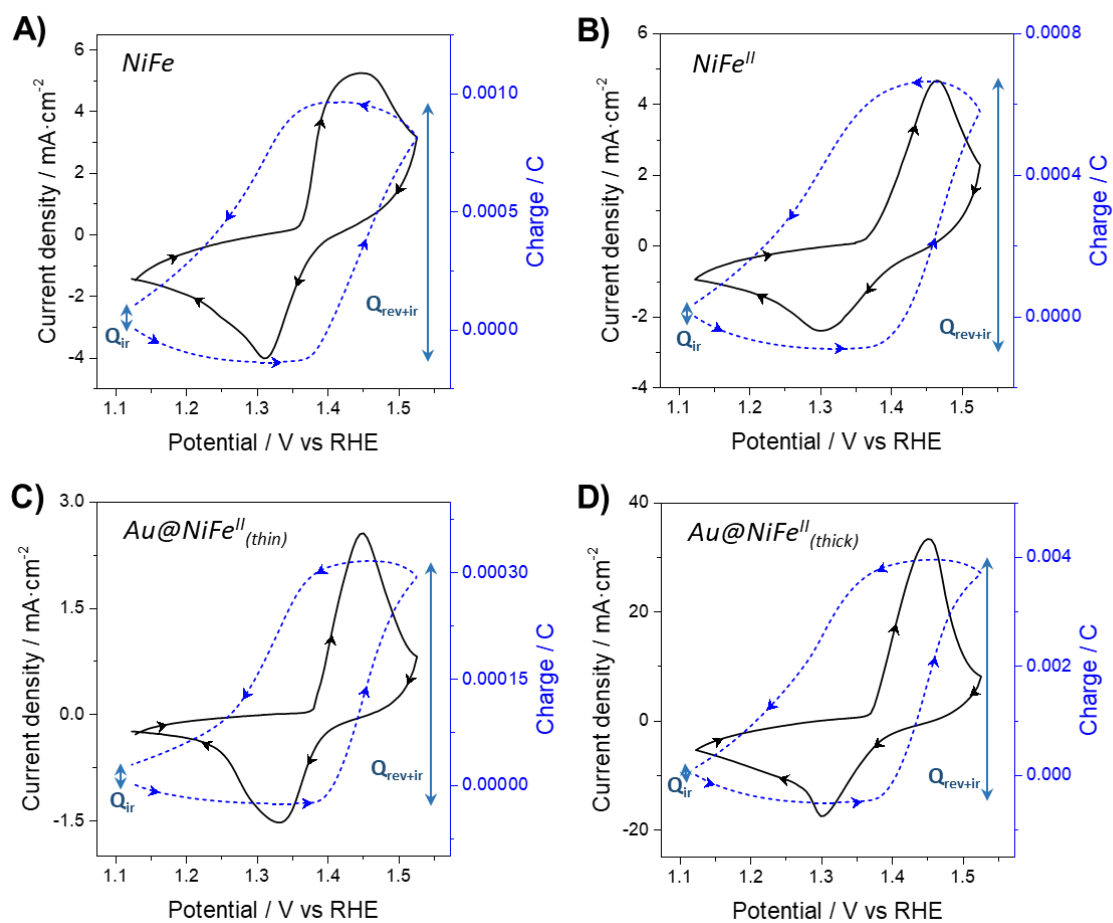
Figure S12. Evolution of the consumed charge (coulovoltammetric response) parallel to the voltammetric response to the cyclic voltammetry performed at 50 mV·s^{-1} in 1 M KOH aqueous solution for NiFe compounds.
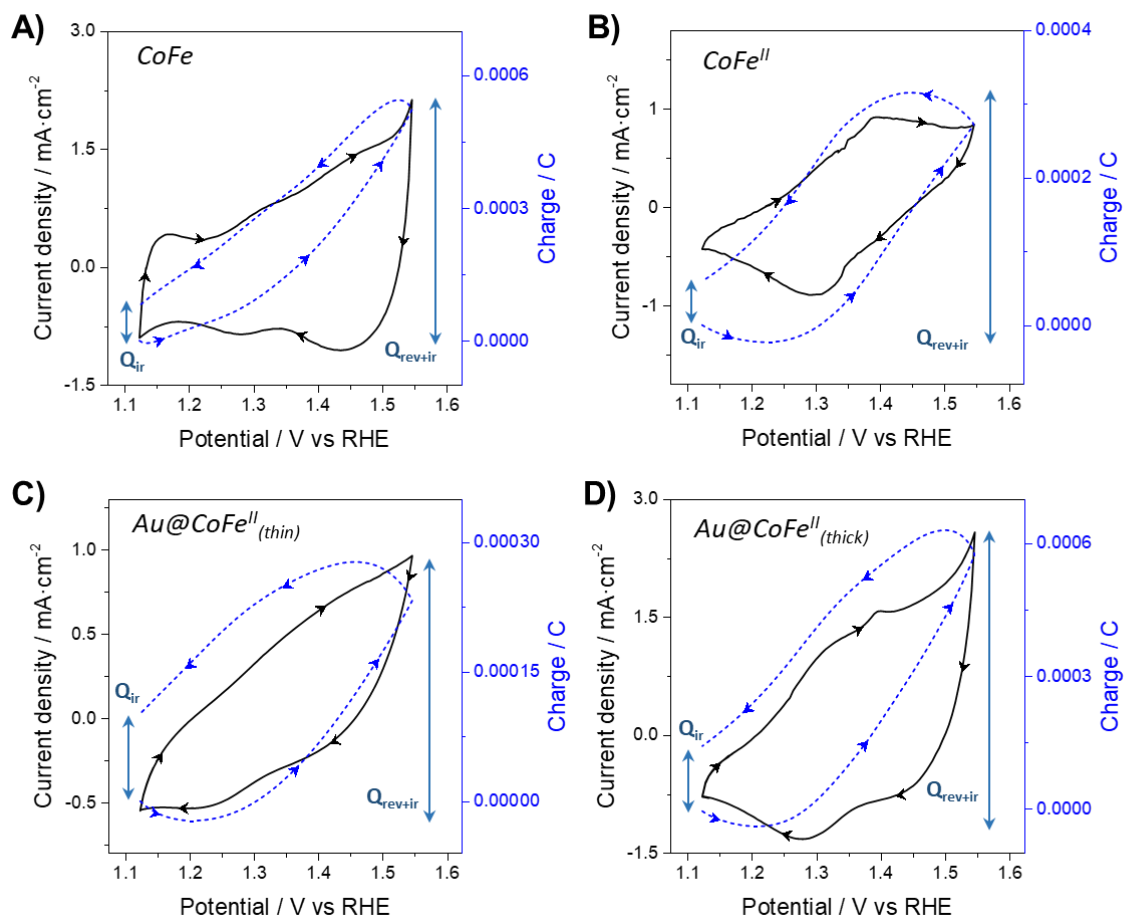
Figure S13. Evolution of the consumed charge during the voltammetric responses to potential cycles performed at 50 mV·s^{-1} in 1 M KOH aqueous solution for CoFe compounds.

Table S3. Amount of electroactive PBA mass being reversibly oxidized/reduced during cyclovoltamperometric experiments.

Samples	PBA mass (mg/cm^2)	z = 1		z = 2	
		PBA e.a. mass (mg/cm^2)	PBA e.a. (%)	PBA e.a. mass (mg/cm^2)	PBA e.a. (%)
NiFe	0.25	0.026	10.2	0.013	5.1
NiFe^{II}	0.25	0.0178	6.4	0.009	3.2
Au@NiFe^{II}$_{(thin)}$	0.14	0.01	8	0.005	4
Au@NiFe^{II}$_{(thick)}$	0.23	0.102	42.4	0.051	21.2
CoFe	0.25	0.0084	3.4		
CoFe^{II}	0.25	0.0071	2.6		
Au@CoFe^{II}$_{(thin)}$	0.12	0.0044	3.2		
Au@CoFe^{II}$_{(thick)}$	0.24	0.0182	7.8		

The electroactive mass (e.a.) of PBA was estimated using Faraday's law of electrolysis:

$$m = \frac{Q}{F} \cdot \frac{M}{z}$$

Being, m the mass (g), Q the charge corresponding to the reversible redox process, M the molecular weight of the sample and z the total number of electrons taking part in the redox process.

Q was calculated by subtracting the total charge involving reversible and irreversible reactions (Q_{rev+ir}) and the charge consumed by the irreversible oxygen evolution, (Q_{ir}) calculated in Figures S12 and S13. The reversible charge allows the calculations of the number of electroactive metal atoms.

The redox processes of NiFe compounds are associated with the oxidation/reduction of Ni. Here, the initial Ni^{2+} is firstly oxidized to a mixed valance state of Ni^{3+}/Ni^{4+}. Therefore, calculations were carried out considering one (z = 1) or two (z = 2) electrons involved in the reaction.

For CoFe compounds, the redox processes associated with the reaction of Co^{2+} and Co^{3+} involves one electron (z = 1).
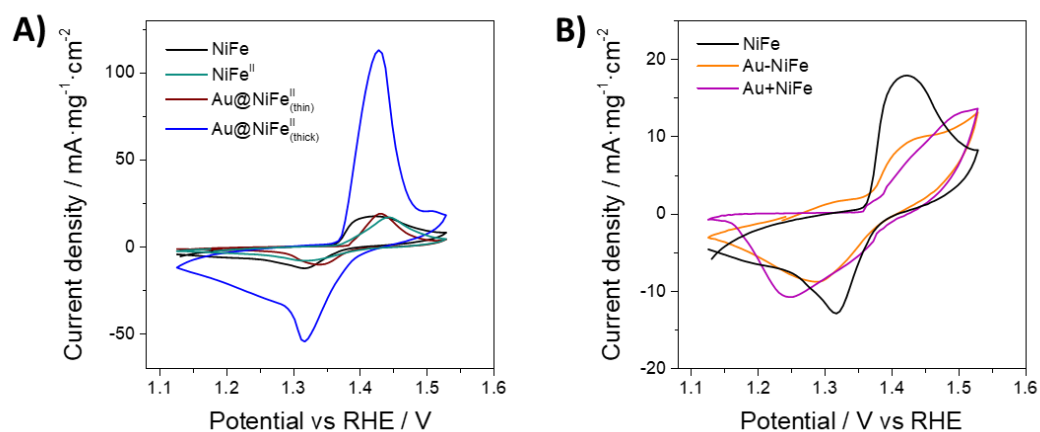
Figure S14. Voltammetric responses to potential cycles performed at 20 mV·s^{-1} in 1 M KOH aqueous solution for NiFe compound compared to: A) NiFe(II) and the electroactive species of Au@NiFe(thin) and Au@NiFe(thick); and B) the electroactive species of Au-NiFe and Au+NiFe.
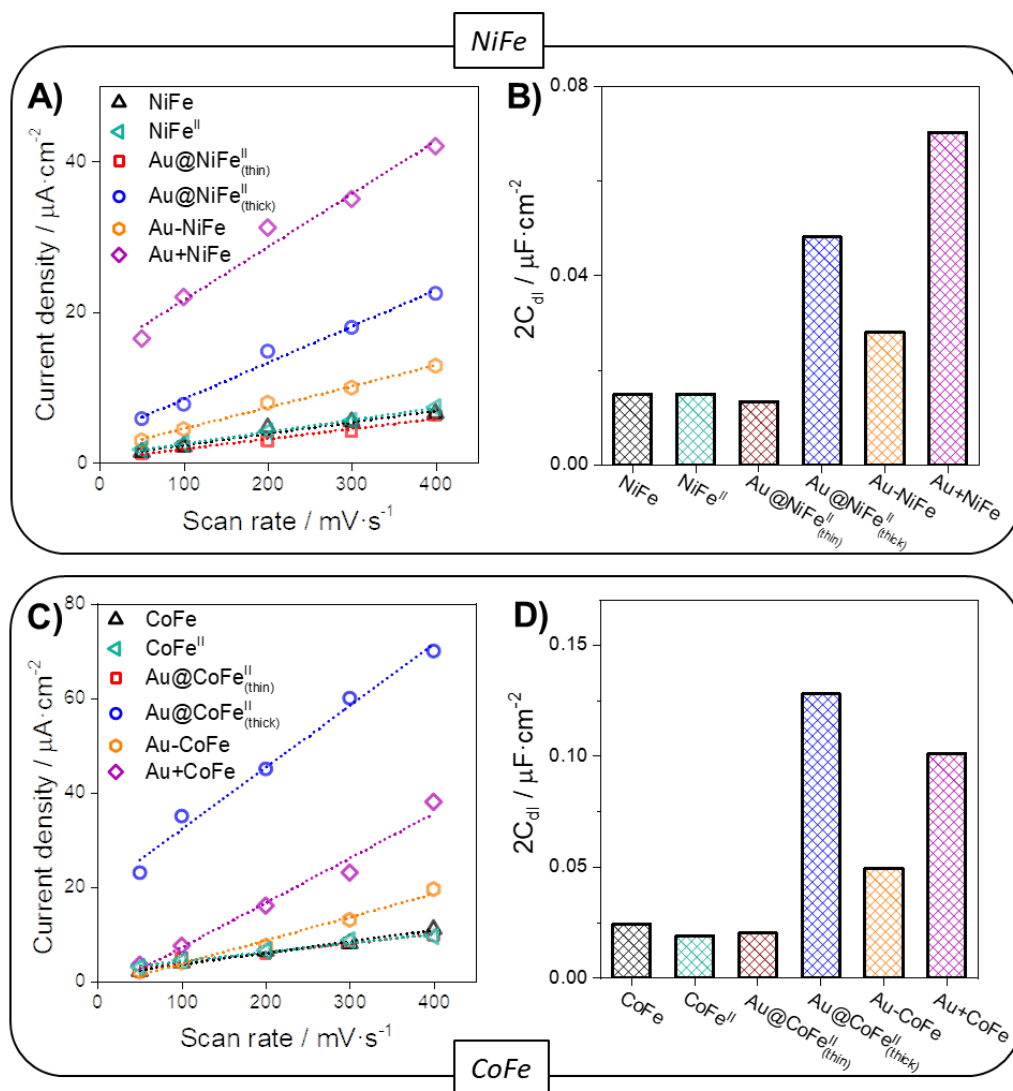
Figure S15. Linear slopes representing the ECSA calculated from CVs performed in a non-faradaic region at different scan rates for NiFe (A) and CoFe (C) PBA compounds. ECSA values of the different NPs of NiFe (B) and CoFe (D) PBA compounds.
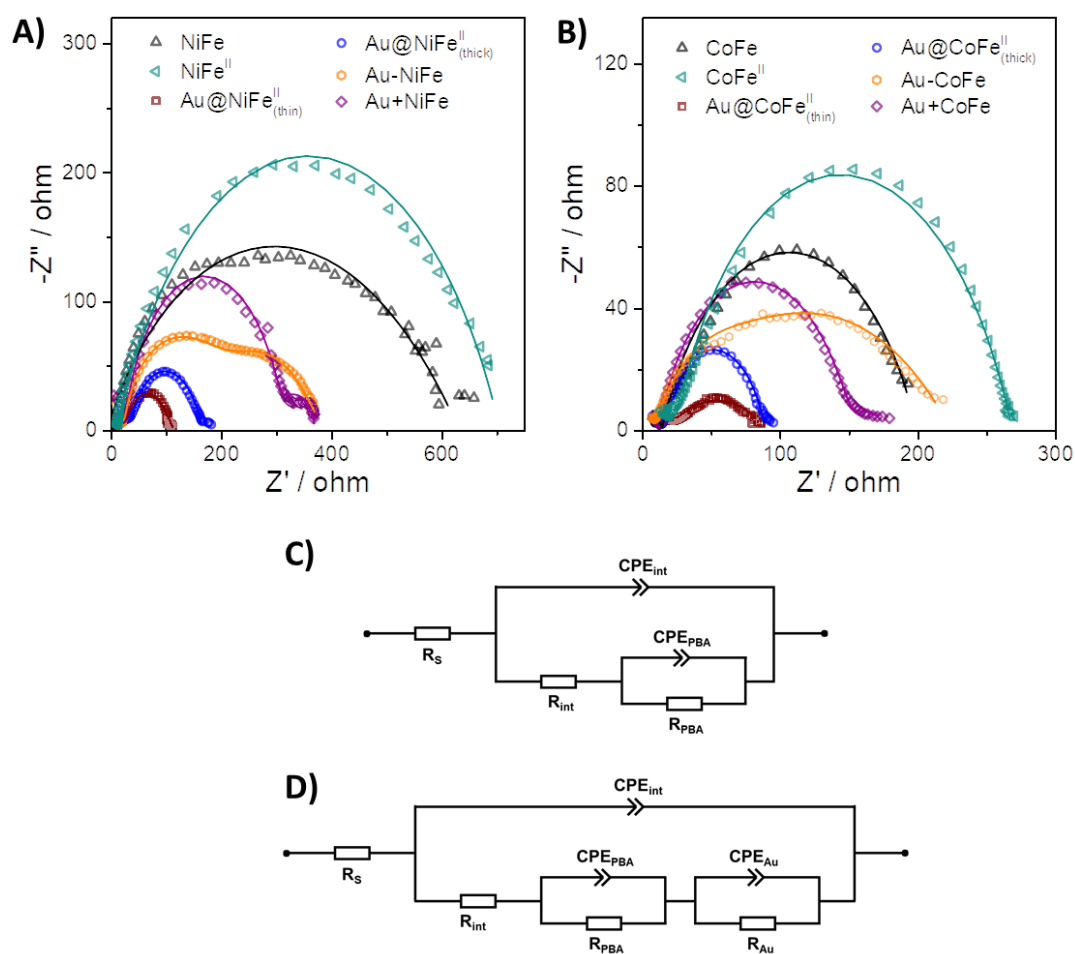
46

Figure S16. A) B) Nyquist plots of the different samples recorded at an overpotential of 0.4 V. Points correspond to experimental data, and lines are curves fitted with the equivalent circuit. C) Equivalent circuit used for the two PBA NPs, Au@PBA(thin) and Au@PBA(thick). D) Equivalent circuit used for Au-PBA and Au+PBA.

Table S4. Comparison of the electrocatalytic activity with previous reported OER electrocatalysts.

| Sample	Overpotential at 10 mA·cm^{-2} (V vs RHE)	Solution	iR correction	Electrode	Reference
Au@NiFe	1.59	1M KOH	no	GC	This work
Au@CoFe	1.57	1M KOH	no	GC	This work
Au@CoO$_4$	1.61	0.1 M KOH	yes	GC	[16]
Au@CoFeO$_x$	1.55	1M KOH	yes	GC	[48]
Au@NiO	1.63	1M KOH	yes	GC	[48]
CoFe-LDH	1.65	1M KOH	no	GC	[45]
NiFe-LDH	1.58	1M KOH	yes	GC	[58]
IrO$_2$	1.57	1M KOH	yes	GC	[58]
CNTs-Au@Co$_3$O$_4$	1.58	1M KOH	no	GC	[49]
NiFe-V$_{CN-}$	1.513	1M KOH	yes	RDE GC	[38]
CoFe-V$_{CN-}$	1.599	1M KOH	yes	RDE GC	[38]
ZnCo$_2$O$_4$/Au/CNTs	1.67	1M KOH	no	RDE GC	[46]
NiO-NiFe$_2$O$_4$/rGO	1.53	1M KOH	no	RDE GC	[53]
CoFe oxide	1.54	1M KOH	yes	Ni foam	[59]
CoFe film	1.66	0.1M KOH	no	FTO glass	[9]
Au/NiFe-LDH	1.467	1M KOH	yes	Ti mesh	[50]
Ag@Co(OH)$_2$	1.48	1M KOH	no	Carbon cloth	[51]
Ag+Co(OH)$_2$	1.55	1M KOH	no	Carbon cloth	[51]
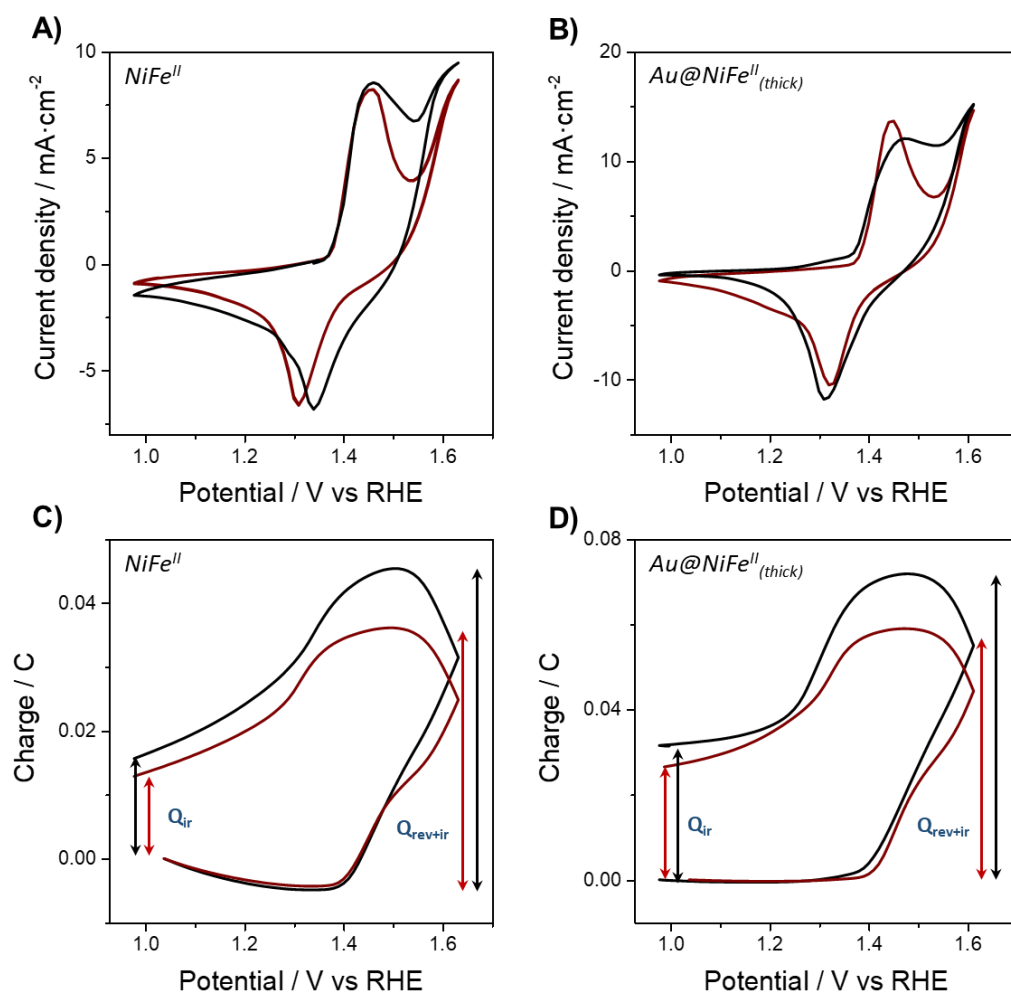
Figure S17. A) B) Voltammetric responses to potential cycles performed at 50 mV·s⁻¹ in 1 M KOH aqueous solution and C) D) evolution of the consumed charge (coulovoltammetric response) parallel to the voltammetric response to the cyclic voltammetry performed at 50 mV·s⁻¹ for NiFe^{II} and Au@NiFe(thick) compounds before and after stability test. Black colors are referred to measurements before stability test and red colors are referred to measurements after stability test.
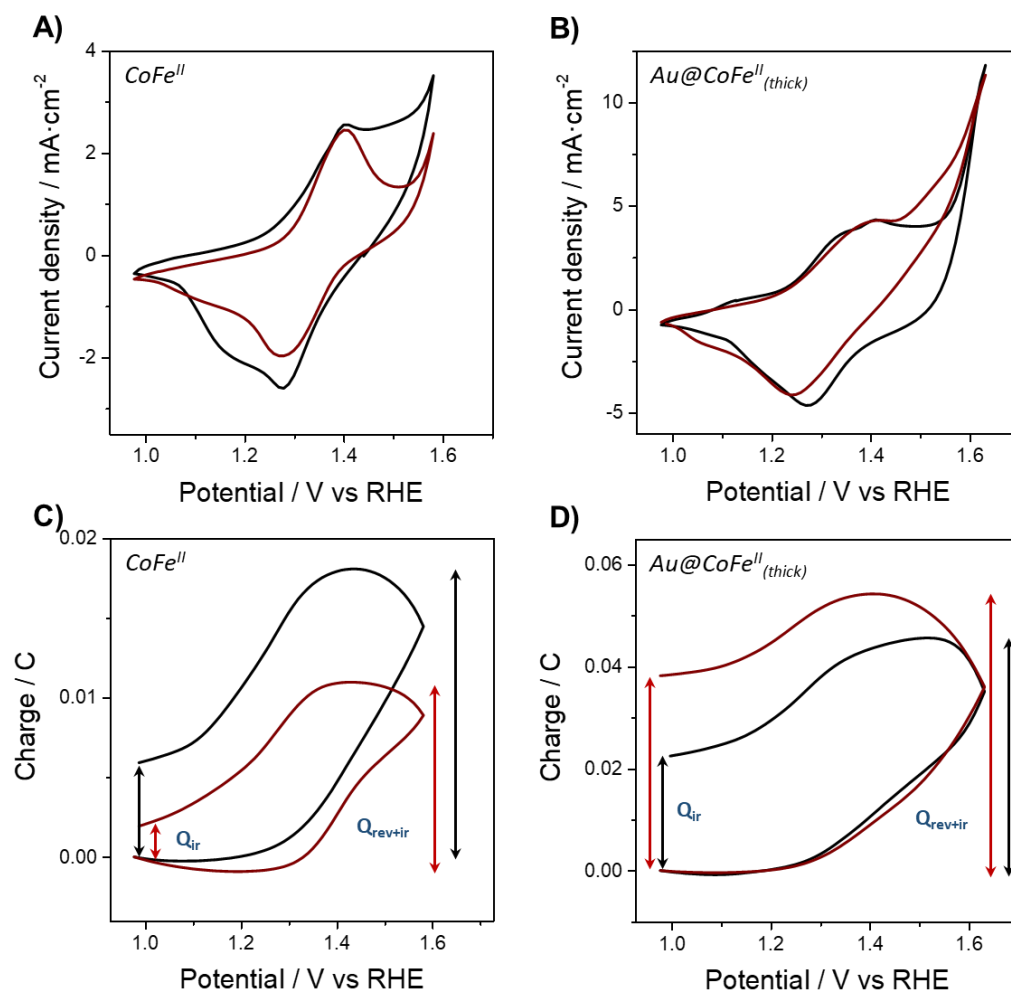
Figure S18. A) B) Voltammetric responses to potential cycles performed at 50 mV·s⁻¹ in 1 M KOH aqueous solution and C) D) evolution of the consumed charge (coulovoltammetric response) parallel to the voltammetric response to the cyclic voltammetry performed at 50 mV·s⁻¹ for CoFe^{II} and Au@CoFe(thick) compounds before and after stability test. Black colors are referred to measurements before stability test and red colors are referred to measurements after stability test.